The Subduction Geometry Beneath Western Washington from Deconvolved Teleseismic *P*-Waveforms

by

David Benjamin Lapp

A thesis submitted in partial fulfillment
of the requirements for the degree of

Master of Science

University of Washington

1987

Approved by _____
(Chairperson of Supervisory Committee)

Program Authorized
to Offer Degree _____

Date _____

Master's Thesis

In presenting this thesis in partial fulfillment of the requirements for a Master's degree at the University of Washington, I agree that the Library shall make its copies freely available for inspection. I further agree that extensive copying of this thesis is allowable only for scholarly purposes, consistent with "fair use" as prescribed in the U.S. Copyright Law. Any other reproduction for any purposes or by any means shall not be allowed without my written permission.

Signature _____

Date _____

TABLE OF CONTENTS

LIST OF TABLES

LIST OF FIGURES

ACKNOWLEDGEMENTS

I wish to thank several people for their assistance. Bob Crosson supported me and helped me to maintain a focus. Ken Creager, Jonathan Lees, John VanDecar and Tony Qamar provided helpful discussion which improved this work. Matthew Hendrickson provided field and data processing procedures, and Tom Owens provided software and innumerable conversations regarding the interpretation. Finally, I owe special thanks to my friends who accompanied me on my field trips, and to Lescenia Arnett.

This work was supported under contract number C-20142, by the Washington Public Power Supply System. Additional support was furnished by the Society of Exploration Geophysicists Education Foundation, to whom I am grateful.

DEDICATION

This work is dedicated
with admiration
to my grandfathers
Louis Greenberg and Benjamin Lapp.

Chapter 1

Introduction

The collision of the Pacific-Farallon ridge with the North American plate between 25 - 30 Ma left the Juan de Fuca plate as an independent tectonic unit in the Pacific northwest (Riddihough, 1984). Present day subduction of the Juan de Fuca (JDF) plate is well accepted due to the existence of deformed sediments on the continental slope and shelf (Carson *et al.*, 1974), and the results of magnetic anomaly analysis (Atwater, 1970; Riddihough, 1984). In addition, the Pacific northwest exhibits a gravity expression typical of a subduction zone environment (Riddihough, 1979).

In the Puget Sound region of western Washington, local seismicity patterns indicate a Benioff zone dipping approximately eastward at 10 - 12 degrees (Crosson, 1983). The observation of teleseismic converted arrivals consistent with a dipping low velocity layer, interpreted as the crust of the subducted JDF plate, at 45 - 50 kilometers depth at WWSSN stations in Corvalis, OR and southern Vancouver Island (Langston, 1981) lend support to large scale subduction. Further seismic studies (Green *et al.*, 1986; Keach *et al.*, 1986) indicating larger slab dips both north and south of Puget Sound have prompted the careful examination of local earthquake hypocenters and teleseismic converted arrivals, resulting in a new 3-dimensional model of the JDF plate beneath western Washington (Crosson and Owens, 1987). The proposed geometry is a subducted slab which is arched in response to a change in azimuth of its trench concentrated over the latitude extent of Puget Sound (47N to 48N).

The analysis of teleseismic converted arrivals recorded at a site south of the Olympic Mountains (Owens *et al.*, 1987a) has provided critical information used in the construction of the new JDF subduction model. This thesis provides the results of a similar analysis using data recorded at a site south of Puget Sound and approximately 60 km east of the station analyzed by Owens *et al.* (1987a). The goal of this study was to assist in the large scale modeling of subduction beneath western Washington by adding local constraints to the subduction geometry beneath southwest Washington. Teleseismic *P* waveforms were processed with a deconvolution scheme which isolates local receiver structure, and then analyzed to determine the local geometry of the JDF slab. Studies such as this, which are aimed towards better understanding of local lithospheric structure, add to our understanding of subduction in the Pacific northwest and will ultimately improve our ability to predict the hazard due to large earthquakes.

Chapter 2

Theory

This thesis involves an investigation of local subduction geometry using broadband teleseismic data. The analysis of converted arrivals resulting from impinging *P* waves formed the basis of interpretation in this study. The motivation for such an analysis is introduced below, followed by a description of the deconvolution technique used to simplify the interpretation.

P-waveform Modeling

The wavetrain composed of a direct *P* wave and its family of scattered (reflected and refracted) *P* and *S* arrivals is referred to as the the *P* waveform. In the presence of vertically heterogeneous structure, the vertical and radial components of a *P* waveform have differences attributable to arrivals emerging as *S* waves (Burdick and Langston, 1977). For *P* waves impinging with constant ray parameter, these waveforms are independent of azimuth. Figure 2.1 displays the synthetic *P* waveform resulting from a flat layer over half-space structure (Table 2.1). Early arrivals are identified using a convention employed by Ammon (1985). The left-most letter (i.e. *P*) represents the impinging *P* wave. Other upper and lower case letters denote downgoing and upgoing paths, respectively. The vertical component contains the direct *P* wave followed by small *P* multiples while the radial is a scaled version of the vertical with the addition of strongly enhanced

Table 2.1

Flat Interface Model

layer #	P wave velocity	S wave velocity	density	thickness	strike	dip
	km/sec	km/sec	g/cm^3	km	degrees	degrees
1	3.0	1.73	2.20	5.0		0.0
2	5.1	2.94	2.60			

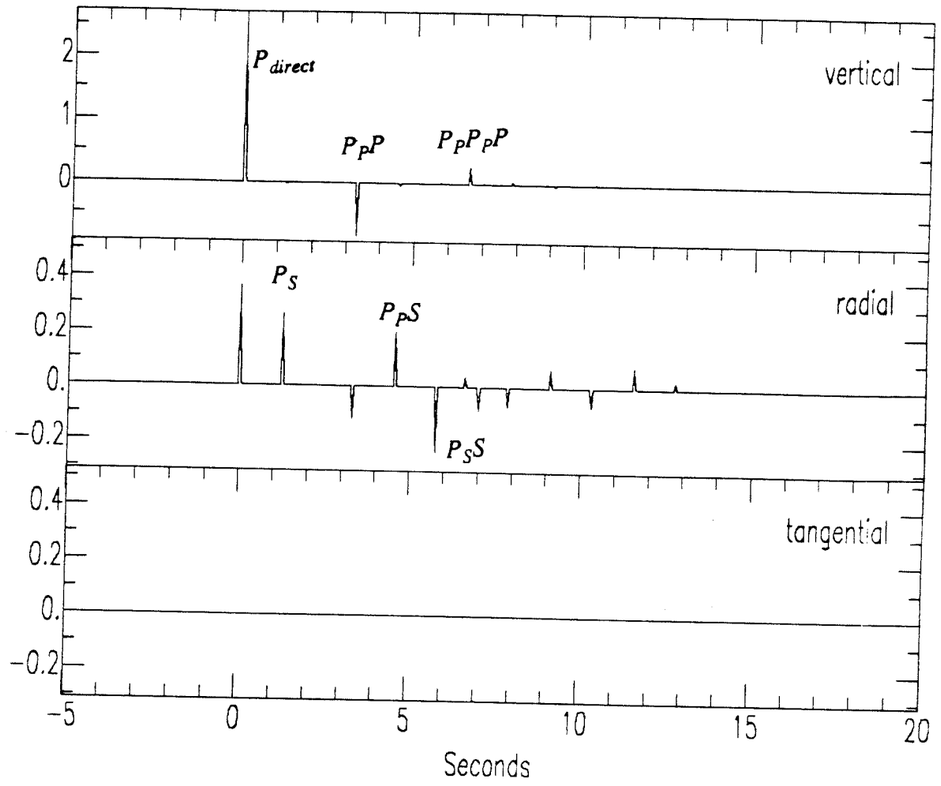

Figure 2.1. Synthetic *P* waveform resulting from a layer over half-space with a flat interface (Table 2.1).

conversions and multiples emerging as *S* waves. In the case of dipping structure, a tangential (off-azimuth) component is generated and the radial *P* waveform minus *S* arrivals is no longer a scaled version of the vertical *P* waveform. This is illustrated by the synthetic *P* waveform shown in Figure 2.2. This *P* waveform resulted from a layer over half-space structure with a dipping interface (see Table 2.2). In addition, azimuthal dependence of the *P* waveform is introduced. Figure 2.3 displays the azimuthal variation in amplitude experienced by the radial component of a direct *P* to *S* conversion through a dipping interface. Arrivals from an updip azimuth (see Figure 2.4) experience efficient *P* to *S* conversion due to the high effective angle of incidence at the dipping interface. The low effective angle of incidence at the dipping interface experienced by downdip azimuth arrivals results in much less efficient conversion. However, as long as arrivals in the *P* waveform impinge on the surface with a small angle of incidence, one can interpret arrivals observed in the radial component, but not prominent in the vertical component, as *S* arrivals in the *P* waveform. Early attempts to constrain receiver structure by modeling converted arrivals in the *P* waveform were hampered by the long period of the data and the need to remove (or at least estimate) the source and path effects which blur the desired local effects (Burdick and Langston, 1977; Langston, 1977a). Because a priori attempts to remove the source generally leave residual effects common to the radial and vertical components, direct interpretation of radial components was difficult. These studies based the interpretation of local *P* to *S* conversions on a comparison of radial to vertical data (Langston, 1977a).

In order to remove source, path, and instrument effects from radial and tangential *P* waveforms, Langston (1979) proposed the method of source equalization. This method allows for the direct interpretation of locally converted arrivals on the resulting "deconvolved receiver function" (see below). The usefulness of the method has been confirmed by several recent studies in which source

Table 2.2

Dipping Interface Model

layer #	P wave velocity	S wave velocity	density	thickness	strike	dip
	km/sec	km/sec	g/cm^3	km	degrees	degrees
1	3.0	1.73	2.20	5.0	0.0	15.0
2	5.1	2.94	2.60			

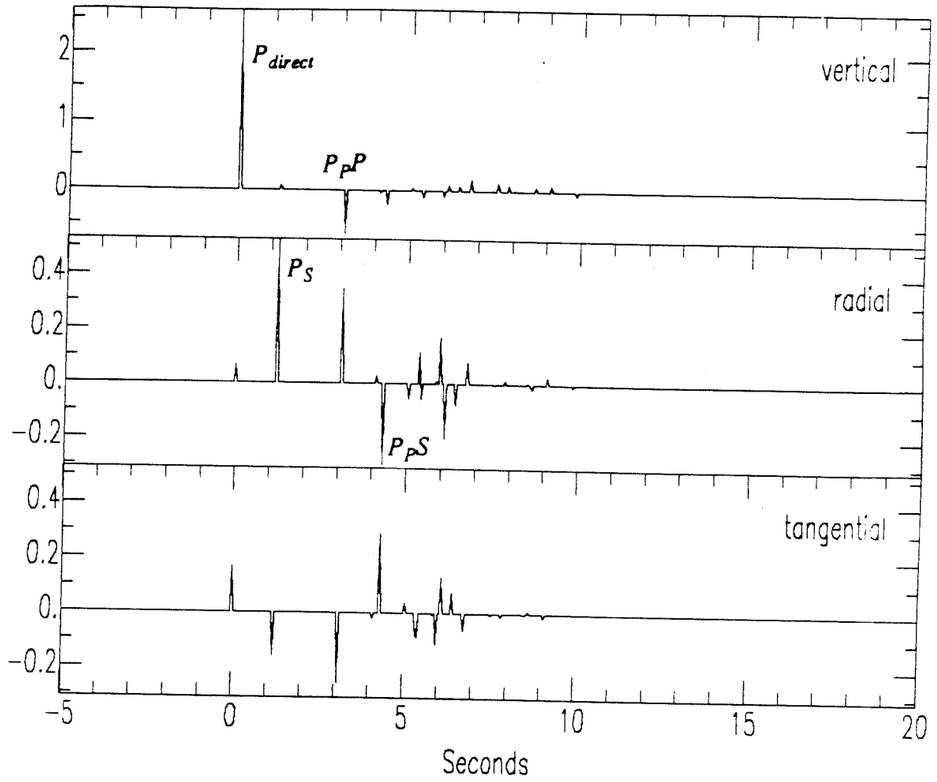

Figure 2.2. Synthetic *P* waveform resulting from a layer over half-space with a dipping interface (Table 2.2).

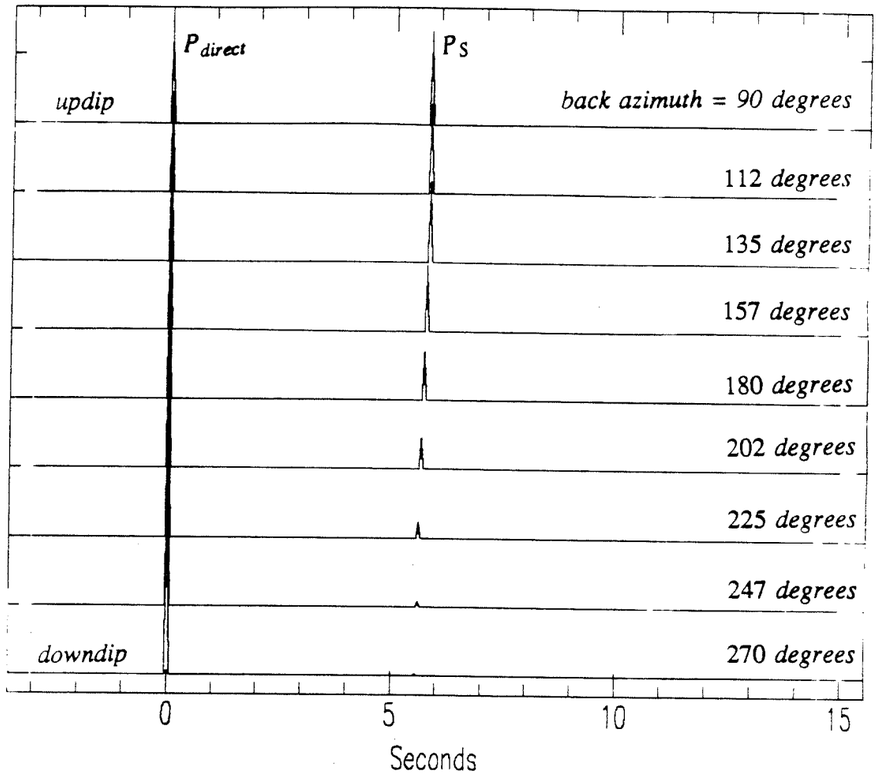

Figure 2.3. Azimuthal variation in the amplitude of the radial componant of a *P* to *S* conversion through a dipping interface. Dip direction is east.

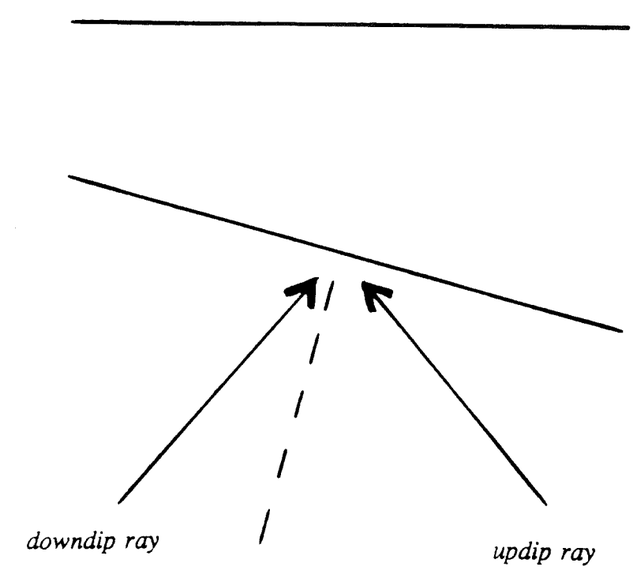

Figure 2.4. Schematic representation of updip and downdip rays.

equalized broadband *P* waveforms were successfully analyzed (see Owens *et al.*, 1985; Owens and Crosson, 1987; Owens *et al.*, 1987a).

Source Equalization

In order to isolate the effects of local crustal and upper mantle structure, source equalization of teleseismic *P* waveforms was performed. Several detailed explanations of source equalization exist (see Langston, 1979; Owens *et al.*, 1983a; Ammon, 1985), thus only a brief description of its theoretical basis will be presented. We assume seismograms due to a steeply incident *P*-wave source function at the base of of the lithosphere represented by the convolutions:

$$M_v(t) = S(t) * R_v(t) * I(t) \tag{2.1a}$$

$$M_r(t) = S(t) * R_r(t) * I(t) \tag{2.1b}$$

$$M_t(t) = S(t) * R_t(t) * I(t) \tag{2.1c}$$

where:

v,r,t = *vertical, radial, tangential respectively*

M = *seismogram*

R = *local receiver function*

S = *local P–wave source function*

I = *instrument response*

Removal of source, path, and instrument effects is achieved by deconvolving the vertical from the radial and tangential components. Time domain deconvolution is represented in the frequency domain as division. Thus, the deconvolution may be represented in the frequency domain as:

$$\frac{M_r(\omega)}{M_v(\omega)} = \frac{I(\omega)S(\omega)R_r(\omega)}{I(\omega)S(\omega)R_v(\omega)} = \frac{R_r(\omega)}{R_v(\omega)} \tag{2.2a}$$

$$\frac{M_t(\omega)}{M_v(\omega)} = \frac{I(\omega)S(\omega)R_t(\omega)}{I(\omega)S(\omega)R_v(\omega)} = \frac{R_t(\omega)}{R_v(\omega)} \qquad (2.2b)$$

Transforming these spectral ratios to the time domain gives the radial and tangential deconvolved receiver functions, which are related to the local radial and tangential lithospheric transfer functions.

Figure 2.5 shows the effect of source equalization on noise-free synthetic data resulting from tracing a steeply incident *P* impulse through a flat layer over half-space structure (see Table 2.1). Early arrivals are identified in Figure 2.1. The radial deconvolved receiver function mimics the radial seismogram except for the removal of multiples emerging as *P* waves and the addition of a few small later arrivals. For instance, the deconvolution removes the 3.3 second *P* multiple but not the 1.2 second *P* to *S* converted arrival (see Figure 2.5). The removal of *P* multiples by source equalization is a result of the radial seismogram containing a scaled version of the vertical seismogram (Langston, 1979).

As discussed earlier, dipping structure results in azimuth-dependent *P* waveforms and the generation of a tangential component of motion. Source equalization of data resulting from dipping structure can result in the survival of *P* multiples. The amount of residual *P*-wave energy in the radial deconvolved receiver function can be large for structures with layers dipping in excess of 10 degrees, and will be highly back azimuth dependent (Ammon, 1985). In addition, the non-zero tangential component of motion yields a deconvolved receiver function. Figure 2.6 displays the effect of dip (see Table 2.2) on the source equalization. Early arrivals are identified in Figure 2.2. Note, in particular, the 3.1 second *P* multiple. The existence of an off-azimuth component to this arrival results in different P_{mult}/P_{direct} amplitude ratios in the radial and vertical components, and the presence of the arrival in the radial deconvolved receiver function. A comprehensive treatment of these effects is given by Langston (1979) and Ammon (1985).

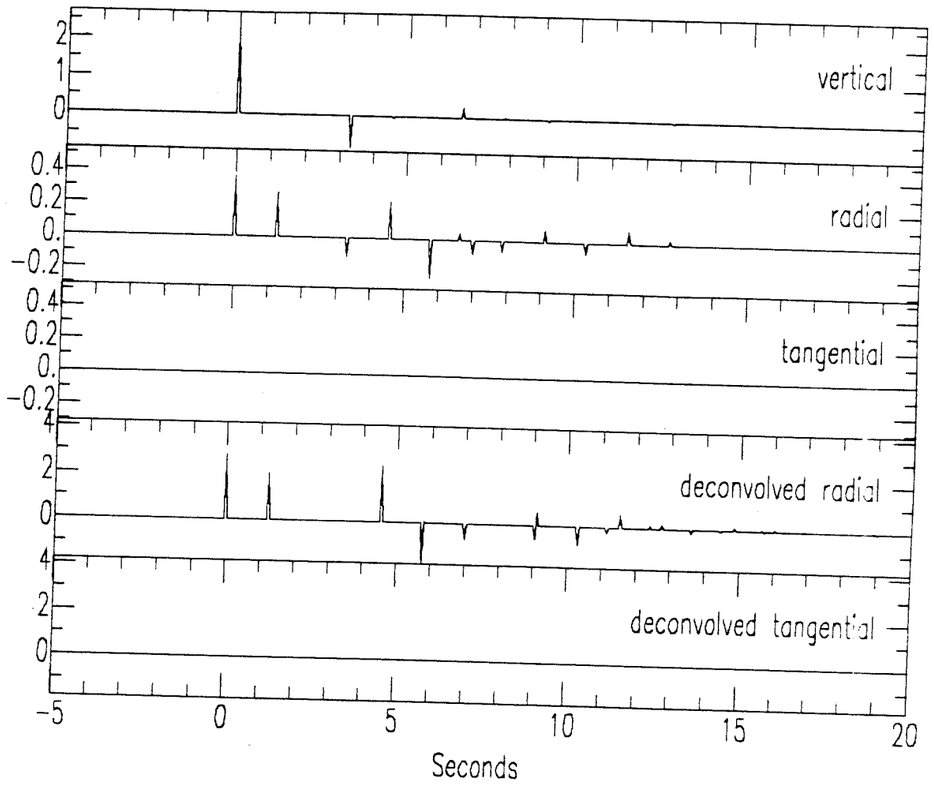

Figure 2.5. Source equalization of a synthetic *P* waveform resulting from a layer over half-space with flat interface (Table 2.1).

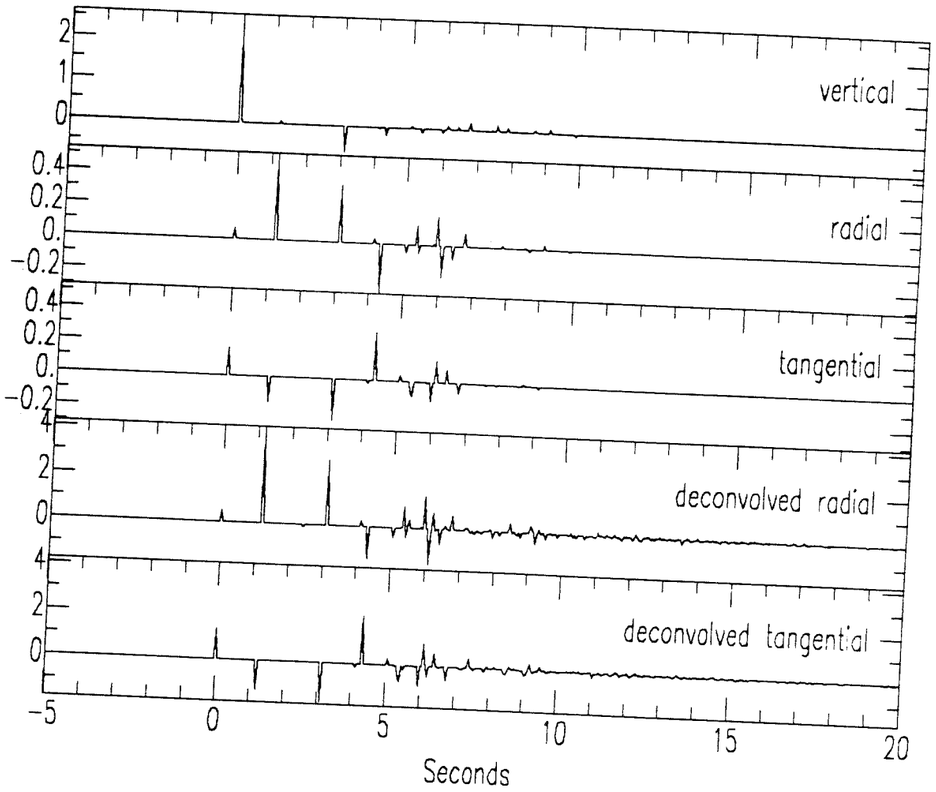

Figure 2.6. Source equalization of a synthetic *P* waveform resulting from a layer over half-space with a dipping interface (Table 2.2).

In the presence of noise, the division in equations 2.2 can be unstable. Spectral troughs in the source function can become misaligned in the radial, tangential, and vertical component spectra, which can result in a small numerator being divided by a much smaller denominator. In order to stablize the source equalization deconvolution, the waterlevel method, proposed by Helmberger and Wiggins (1971), was employed. The numerator and denominator of equations 2.2 are multiplied by the complex conjugate of $M_v(\omega)$, $M_v^*(\omega)$, and the resulting denominator is not allowed to take on values below a specified fraction of the denominator's maximum across the entire spectrum:

$$\frac{M_r(\omega)}{M_v(\omega)} \approx \frac{M_r(\omega)M_v^*(\omega)}{max[M_v(\omega)M_v^*(\omega)\ ,\ c \cdot MAX\ \{M_v(\omega)M_v^*(\omega)\}]} \tag{2.3a}$$

$$\frac{M_t(\omega)}{M_v(\omega)} \approx \frac{M_t(\omega)M_v^*(\omega)}{max[M_v(\omega)M_v^*(\omega)\ ,\ c \cdot MAX\ \{M_v(\omega)M_v^*(\omega)\}]} \tag{2.3b}$$

max = *maximum at each* ω

MAX = maximum reached over entire spectrum

c = waterlevel

To avoid high frequency noise, equations 2.3 are multiplied by a Gaussian low pass filter, represented in the frequency domain as :

$$G(\omega) = e^{-\omega^2/4a^2} \tag{2.4}$$

where a is the Gaussian parameter. Whenever possible, deconvolved receiver functions from events within a specified epicentral range were stacked. The range used was that suggested by Owens *et al.* (1983a):

± 20 *degrees in back azimuth*

± 15 *degrees in distance for distance > 70 degrees*

± 10 *degrees in distance for distance < 70 degrees*

Figure 2.7 demonstrates the coherence of radial deconvolved receiver functions which were derived from non-coherent raw data. The epicenters of these events were within the stackable range listed above. The raw seismograms from these events do not display consistent features, while the deconvolved receiver functions are highly coherent.

In this thesis, the relative timing and amplitudes of arrivals persistently observed in radial deconvolved receiver functions were synthetically reproduced by means of forward modeling. The goal was to constrain local subduction geometry. Tangential data tend to be smaller amplitude (lower *signal/noise*) than radial data, and generally less stable (Langston, 1981), making interpretation very difficult without extensive azimuthal coverage. Because this coverage was not obtained, tangential data were not modeled. Synthetic seismograms were generated with a 3-dimensional ray tracing routine which allows moderately dipping planar interfaces (Langston, 1977b). The output of this routine has been checked in the case of flat layers by comparison to the output of a program using the Thomson-Haskell method, which gives a complete solution to the equations of motion (Hendrickson, 1986). The synthetic seismograms were deconvolved in the same manner as the real data, and the synthetic structure was modified to fit the data.

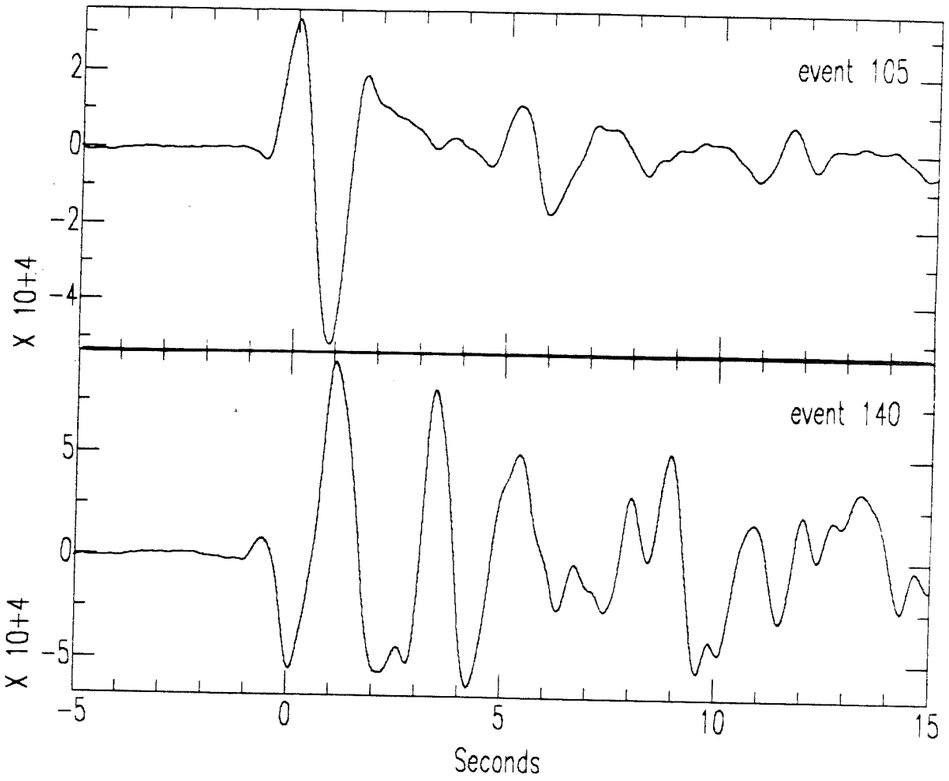

Figure 2.7a. Vertical seismograms from events 105 and 140.

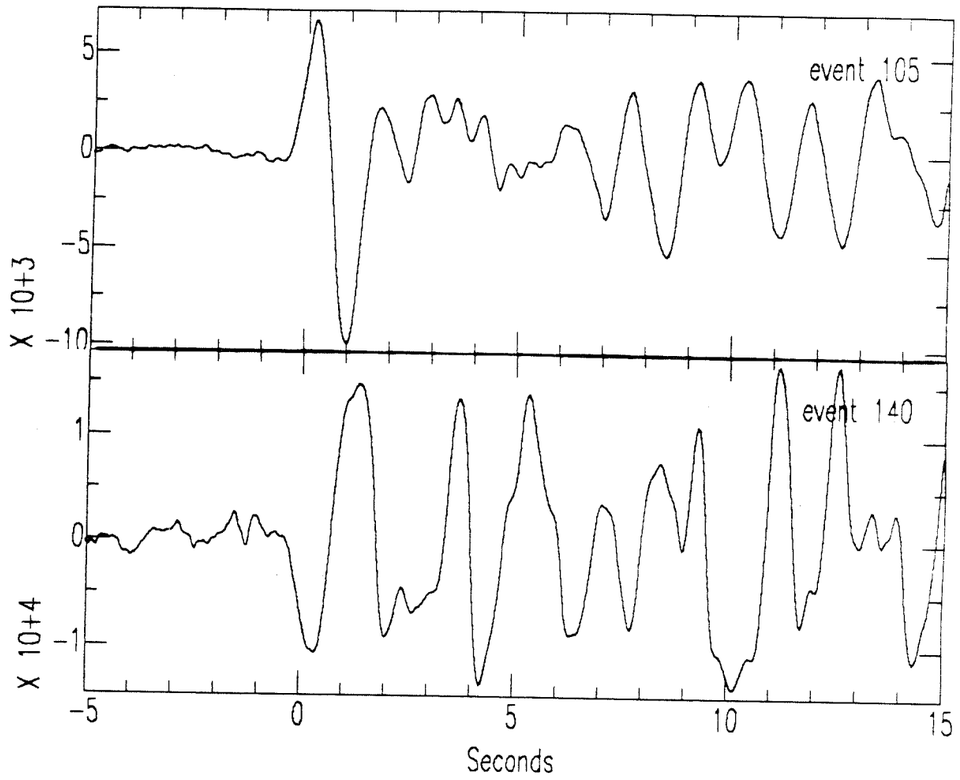

Figure 2.7b. Radial seismograms from events 105 and 140.

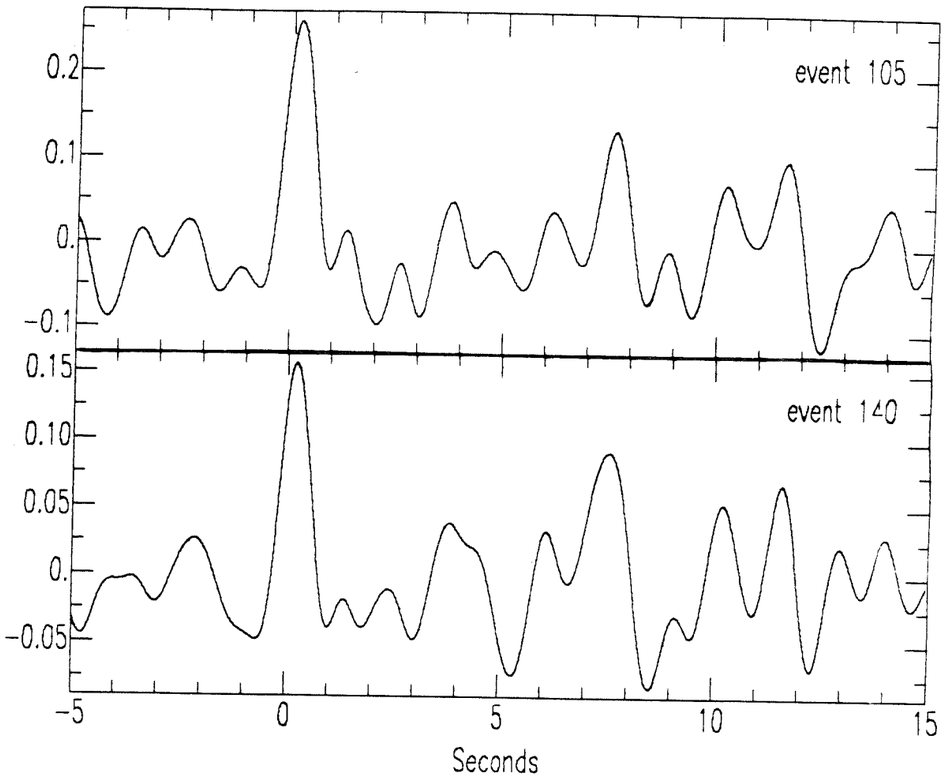

Figure 2.7c. Radial deconvolved receiver functions from events 105 and 140 displaying the removal of blurring effects.

Chapter 3

Data Collection and Processing

Temporary seismic stations recording three components of digital broadband data have been deployed in southwest Washington since August, 1984. Until the early summer of 1986, the array configuration was a tight cluster of stations located south of the Olympic mountains. Presently, the stations are situated in an approximately linear array (running east-west) with spacing of roughly 30 km. The array extends from the original array location to approximately 30 km east of Mt. Rainier. The station numbers of the original sites were 1 through 5. Currently, sites are numbered 4, 6, 7 and 8, where site 4 was part of the original array. Figure 3.1 displays the current array configuration. The station locations are given in Table 3.1. The basement Paleogene basalts underlying the stations probably accumulated in seamounts near the coast of North America and were tectonically accreted onto the coast ranges of Washington about 40 Ma (Cowan and Potter, 1986).

Each station was equipped with intermediate period (5 second) Kinemetrics SH-1 and SV-1 velocity seismometers. Resistance was installed in each seismometer to give .7 critical damping. A Sprengnether DR-200 digital recording unit was used at each site to record data digitally at 20 hertz onto 4 tracks of cassette tape. Signals were conditioned with a gain of 60 db and a Butterworth lowpass filter having a corner frequency of 6.25 hertz for anti-aliasing (Nyquist frequency = 10 hertz). Nominal frequency response (i.e. seismometer and Butterworth low-pass filter effects) is illustrated in Figure 3.2. Triggering was accomplished with a $\frac{\textit{short term average}}{\textit{long term average}}$ (referred to as *sta/lta*) specification. When the absolute value

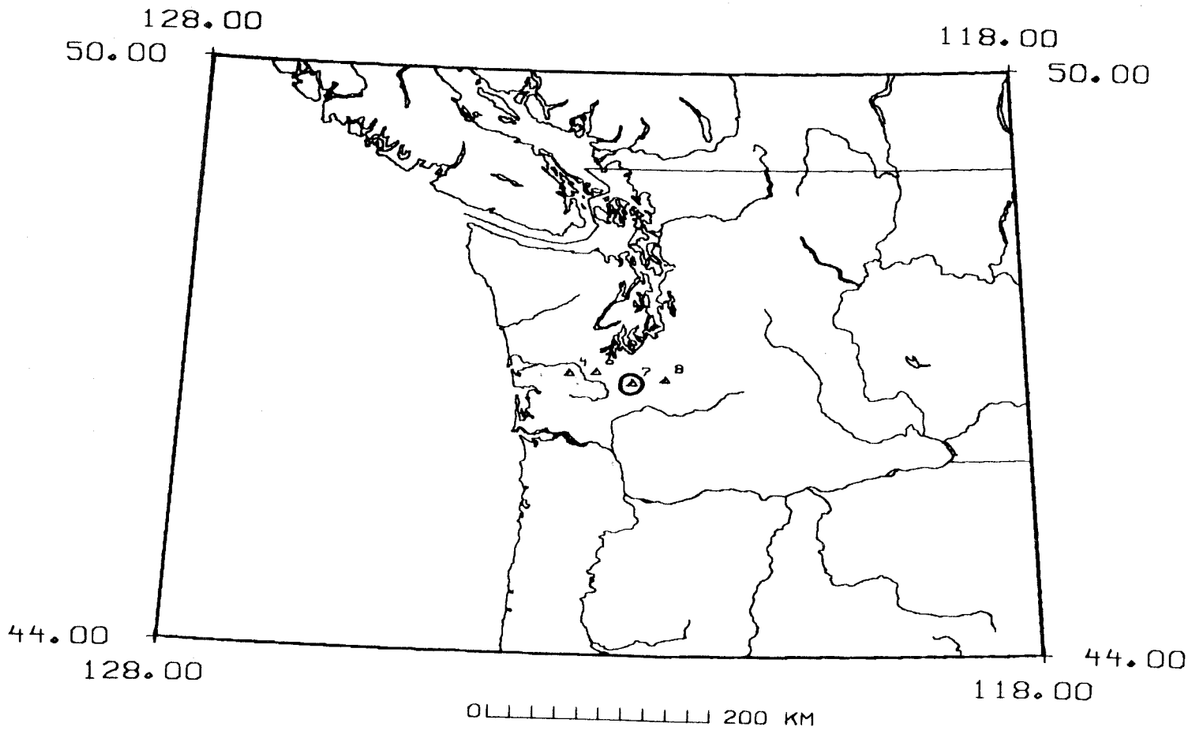

Figure 3.1. Broadband array configuration; site 7 (circled) is analyzed in this study.

Table 3.1

Station locations

Station #	Site	Latitude	Longitude
4	Minot Peak	46.895N	123.417W
6	Capitol Forest	46.914N	123.114W
7	Miller Hill	46.802N	122.684W
8	Pack Forest	46.839N	122.297W

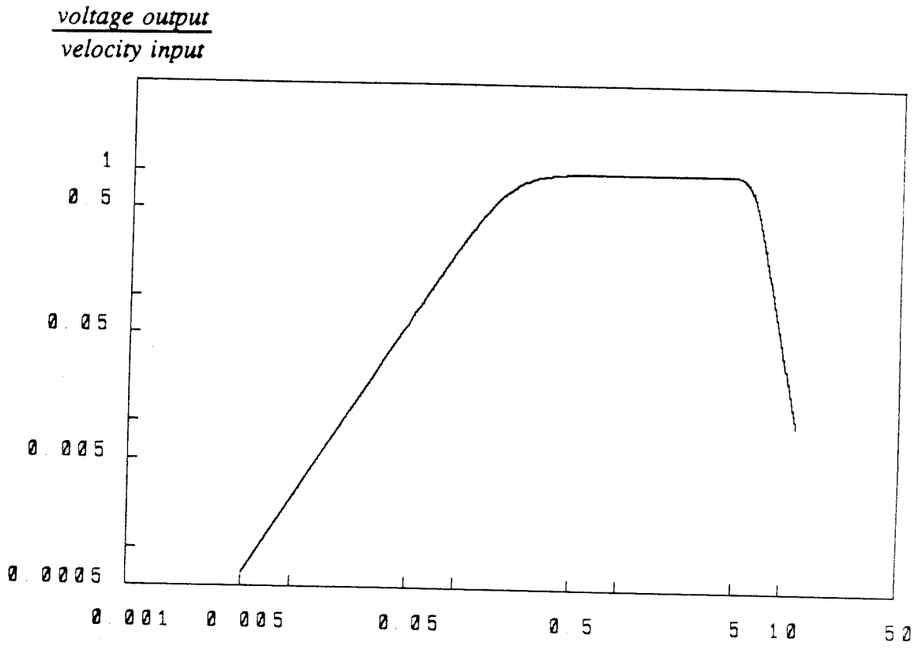

Figure 3.2. Nominal frequency response.

of amplitude summed over the short term divided by the absolute value of amplitude summed over the long term exceeds a specified value, recording begins. Recording continues until the *sta/lta* falls below the specified value. Seasonal variation of the *sta/lta* triggering value was necessary because of changing noise sources. In the late fall and early winter months, the dominant source of false triggers was storm related noise and a generally high level of wind-related background noise. The desired teleseisms usually had a higher frequency content than much of this noise, so the short and long terms were specified in order to desensitize the triggering to low frequency signals (i.e. frequency << 1 hertz). The winter triggering parameters were a short term of 1.6 seconds, a long term of 25.4 seconds, and a ratio of 9 db. During the summer months, background noise was less severe and local blasting, which acts as a source of high frequency noise, was very common. Thus, the short and long terms were each broadened so that the triggering would be desensitized to high frequency signals (i.e. frequency >> 1 hertz). The summer triggering parameters were a short term of 6.4 seconds, a long term of 102 seconds, and a ratio of 6 db. Since the desired teleseisms impinge on the surface with a small angle of incidence, the *sta/lta* triggering requirement was on the vertical component only. Pre-event and post-event durations of 33 seconds and 100 seconds, respectively, were saved to tape. For details regarding seismometer calibration and recorder instrumentation, see Hendrickson (1986).

Cassette tapes from the field were played back with a Sprengnether DP-250 playback unit onto an IBM PC-XT and transferred to a Ridge 32C computer for inspection and analysis. Each event file was viewed and anything resembling a teleseism was saved. The trigger times of saved events (which are accurate to better than 2 seconds) were compared to Preliminary Determination of Epicenter (PDE) listings for location. Generally, only teleseisms of magnitude 5.0 or greater

were recorded, making identification of events in the PDE listings quite easy. Station chronologies are listed in Table 3.2 and represented in Figure 3.3. Events recorded are listed in Table 3.3. Events were numbered from 100 so that events 1 through 59 in Hendrickson (1986) could be referred to without confusion.

Once the recorded teleseisms were located, their horizontal components were rotated into radial and tangential orientations. The radial and tangential components were source equalized (see Chapter 2) using the waterlevel values .0001, .001, .01, and .1 (see Equations 2.3), and a Gaussian parameter of 5.0 (see Equation 2.4). Using a Gaussian parameter of 5.0 decreased the effective roll-off frequency of the system response from 6.25 hertz (see Figure 3.2) to approximately 1 hertz. This helped to prevent contamination due to high frequency noise. Owens *et al.* (1983a) discuss the effects of varying the waterlevel and Gaussian parameter upon a deconvolved receiver function. Deconvolved receiver functions with high *signal/noise* were picked for analysis. Figure 3.4 illustrates the effect of waterlevel upon the quality of radial deconvolved receiver functions for events 102 and 139. The deconvolutions of both events are unstable without a waterlevel. The deconvolution of event 102 displays an improved *signal/noise* when the waterlevel is increased, while the deconvolution of event 139 shows less improvement. In this case, event 102 would be picked for analysis and event 139 would not be used.

Extensive analysis of data recorded in the vicinity of site 4 has been performed by Hendrickson (1986) and Owens *et al.* (1987a). Hence, the small number of events recorded at site 4 were not used in the analysis. Because of the contamination of data recorded at site 6 (see Chapter 4) and the extremely limited amount of data recorded at site 8, only data recorded at site 7 were used in the analysis. As mentioned earlier, radial data tends to be more stable than tangential data in the presence of noise. This was the case for the data used in this study. Because of the lack of azimuthal coverage and low *signal/noise* of the tangential

Table 3.2a

Station 4 chronology

On	Off	Reason for failure
8/20/86	8/26/86	Seismometer malfunction
10/15/86	11/15/86	Recorder malfunction
12/11/86	12/23/86	Noise filled tape
1/27/87	3/ 6/87	Batteries dead

Table 3.2b

Station 6 chronology

On	Off	Reason for failure
6/20/86	7/14/86	Recorder malfunction
8/ 6/86	8/20/86	Seismometer malfunction
9/11/86	9/22/86	Tape filled
9/26/86	11/ 5/86	Tape filled
11/15/86	11/24/86	Tape filled
12/11/86		

Table 3.2c

Station 7 chronology

On	Off	Reason for failure
7/ 6/86	8/ 4/86	Recorder malfunction
8/15/86	9/10/86	Noise filled tape
9/26/86	10/ 9/86	Noise filled tape
10/17/86	12/11/86	Recorder malfunction

Table 3.2d

Station 8 chronology

On	Off	Reason for failure
8/15/86	12/ 4/86	Recorder malfunction
1/27/87	2/ 7/87	Seismometer malfunction

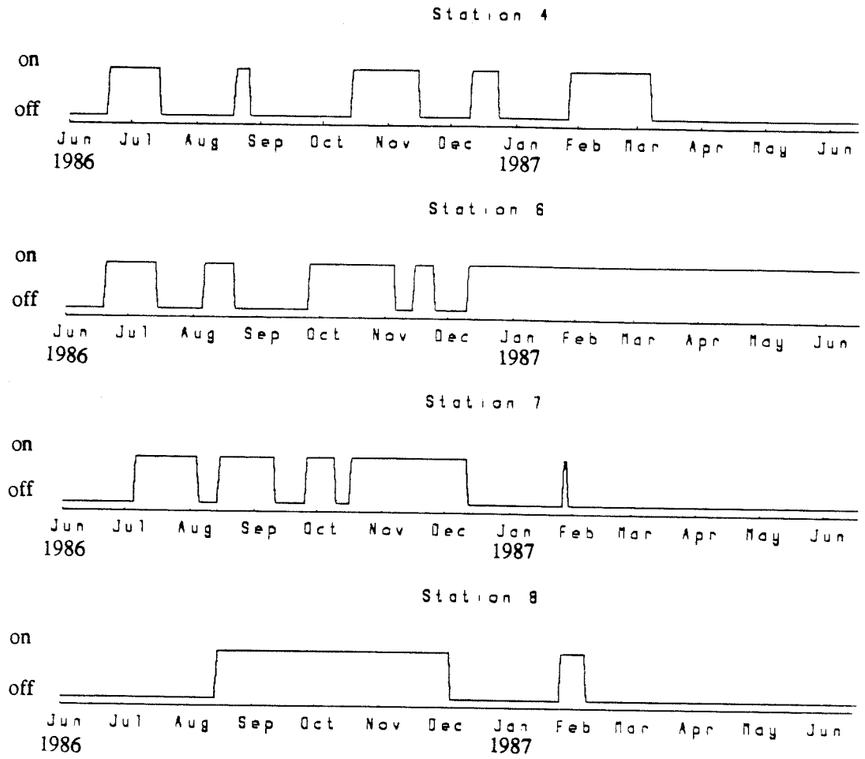

Figure 3.3. Station chronologies.

Table 3.3a

Events recorded at site 4

event#	date	mag.	dist.	depth	baz.	lat.	lon.
100	6/11/86	6.0	78.3	34.	119.4	10.602S	62.949W
137	10/20/86	6.0	88.8	33.	225.1	28.100S	176.430W
140	10/30/86	6.0	83.6	194.	228.8	21.693S	176.679W
141	11/14/86	6.0	88.4	33.	304.0	23.963N	121.822E
142	11/14/86	6.0	88.4	33.	304.0	23.880N	121.817E

Table 3.3b

Events recorded at site 6

event#	date	mag.	dist.	depth	baz.	lat.	lon.
124	8/14/86	6.0	102.4	43.	286.3	1.186N	126.637E
125	8/18/86	5.0	81.3	33.	227.7	20.373S	174.348W
128	9/12/86	6.0	20.8	33.	307.7	56.211N	153.344W
129	9/13/86	5.0	93.5	243.	225.7	31.647S	179.967W
130	9/15/86	5.0	83.8	33.	227.2	22.711S	175.327W
131	9/16/86	6.0	76.5	83.	83.8	19.285N	146.334E
132	9/16/86	5.0	49.7	33.	13.5	56.369N	153.292E
133	10/ 1/86	5.0	34.1	33.	297.9	51.710N	175.941W
136	10/18/86	5.0	84.0	45.	281.2	12.129N	142.859E
137	10/20/86	6.0	88.8	33.	225.1	28.100S	176.430W
138	10/21/86	5.0	88.6	33.	225.3	27.820S	176.524W
139	10/22/86	5.0	85.0	202.	248.8	10.634S	166.029E
145	1/ 5/87	6.0	30.0	33.	297.9	52.455N	169.345W
146	1/ 6/87	5.0	88.4	38.	304.0	23.991N	121.781E
147	1/ 9/87	6.0	65.5	98.	302.5	39.786N	141.615E
148	1/14/87	6.0	62.9	99.	304.1	42.558N	142.879E
149	1/21/87	5.0	76.6	124.	285.8	20.608N	144.829E
150	2/10/87	6.1	82.2	397.	230.7	19.445S	177.479W
151	2/11/87	5.8	88.1	72.	244.5	15.818S	167.262E
152	2/14/87	5.7	81.5	570.	232.6	17.832S	178.723W
153	2/18/87	6.2	36.3	33.	298.2	51.312N	179.306W
154	2/27/87	6.0	28.7	33.	299.8	53.510N	167.362W
155	3/ 5/87	6.6	85.6	28.	133.2	24.515S	70.167W
156	3/ 6/87	6.0	61.2	14.	125.5	0.119N	77.661W
157	3/ 6/87	6.5	61.0	33.	125.6	0.225N	77.764W

Table 3.3b (Continued)

Events recorded at site 6

event#	date	mag.	dist.	depth	baz.	lat.	lon.
158	3/18/87	6.7	76.6	33.	302.6	32.018N	131.639E
159	4/ 1/87	6.2	86.3	272.	129.2	22.781S	66.179W

Table 3.3c

Events recorded at site 7

event#	date	mag.	dist.	depth	baz.	lat.	lon.
101	6/14/86	5.0	89.1	33.	240.5	19.174S	169.826E
102	6/16/86	6.0	85.0	565.	230.6	21.897S	179.083W
103	6/24/86	6.0	95.2	121.	269.1	4.424S	143.979E
104	6/24/86	5.0	89.8	33.	226.3	28.246S	178.200W
105	6/28/86	6.0	81.9	250.	229.3	19.990S	176.078W
106	6/29/86	4.0	33.3	33.	298.8	52.330N	174.850W
107	6/29/86	5.0	89.5	33.	226.3	27.961S	177.982W
108	6/29/86	5.0	69.4	159.	125.5	6.787S	73.001W
109	6/30/86	5.0	47.3	62.	126.5	11.216N	86.090W
110	7/ 1/86	5.0	76.4	33.	228.6	15.673S	172.326W
111	7/ 5/86	5.0	36.6	33.	298.2	51.253N	179.768W
112	7/ 5/86	5.0	40.3	117.	130.7	15.503N	92.505W
113	7/ 7/86	6.0	122.9	10.	0.1	10.421N	56.784E
114	7/ 8/86	5.0	13.8	10.	156.8	33.998N	116.607W
115	7/ 9/86	5.0	34.3	52.	298.4	51.911N	176.288W
116	7/ 9/86	6.0	102.3	53.	286.4	1.956N	126.593E
117	7/19/86	5.0	19.1	151.	281.2	47.223N	151.130W
118	7/19/86	5.0	28.6	33.	299.9	53.568N	167.210W
119	7/19/86	5.0	28.7	33.	299.9	53.557N	167.328W
120	7/20/86	5.0	9.9	8.	158.0	37.580N	118.450W
121	7/21/86	4.0	4.4	10.	224.7	43.682N	127.411W
122	7/21/86	6.0	10.0	9.	158.1	37.537N	118.447W
123	7/21/86	5.0	10.0	9.	158.0	37.498N	118.397W
125	8/18/86	5.0	81.3	33.	227.7	20.373S	174.348W
134	10/ 6/86	5.0	34.3	45.	298.3	51.843N	176.307W

Table 3.3c (Continued)

Events recorded at site 7

event#	date	mag.	dist.	depth	baz.	lat.	lon.
135	10/ 7/86	5.0	73.2	394.	298.7	31.862N	137.648E
139	10/22/86	5.0	85.0	202.	248.8	10.634S	166.029E
140	10/30/86	6.0	83.6	194.	228.8	21.693S	176.679W
141	11/14/86	6.0	88.4	33.	304.0	23.963N	121.822E
142	11/14/86	6.0	88.4	33.	304.0	23.880N	121.817E
143	11/21/86	5.0	6.6	15.	188.9	40.372N	124.443W
144	11/23/86	6.0	64.1	126.	127.5	3.358S	77.474W

Table 3.3d

Events recorded at site 8

event#	date	mag.	dist.	depth	baz.	lat.	lon.
126	8/30/86	6.0	84.1	139.	21.1	45.550N	26.302E
127	8/31/86	5.0	75.3	33.	288.1	23.140N	144.133E
128	9/12/86	6.0	20.8	33.	307.7	56.211N	153.344W
129	9/13/86	5.0	93.5	243.	225.7	31.647S	179.967W
130	9/15/86	5.0	83.8	33.	227.2	22.711S	175.327W
131	9/16/86	6.0	76.5	83.	283.8	19.285N	146.334E
132	9/16/86	5.0	49.7	33.	313.5	56.369N	153.292E

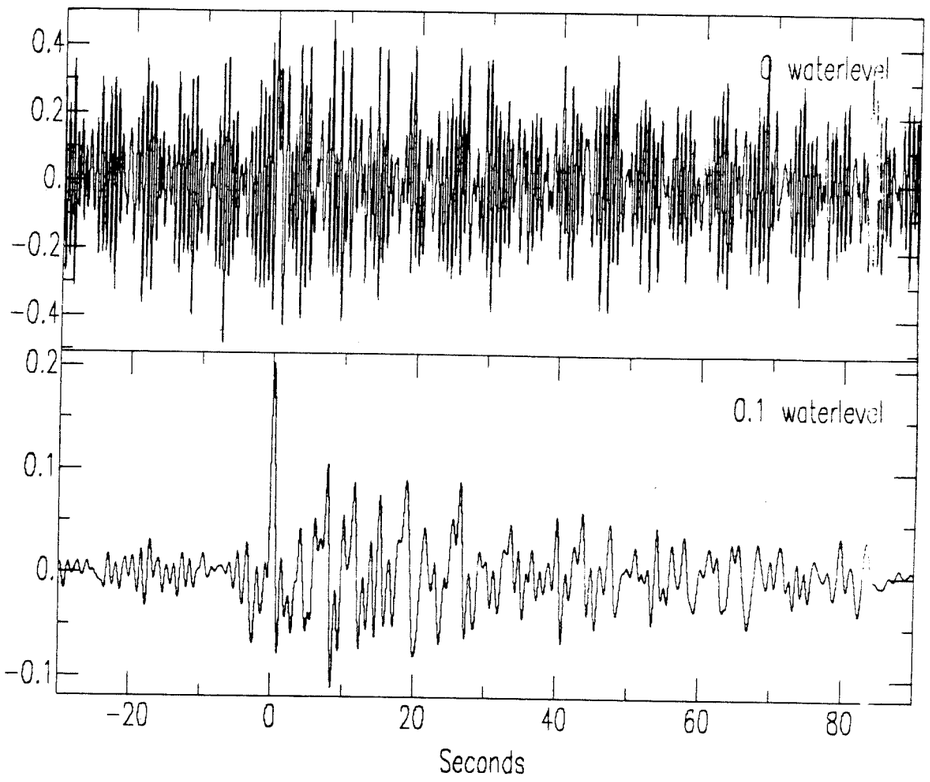

Figure 3.4a. Source equalization of event 102 using a Gaussian parameter of 5.0 and waterlevels of 0 (top trace) and 0.1 (bottom trace) .

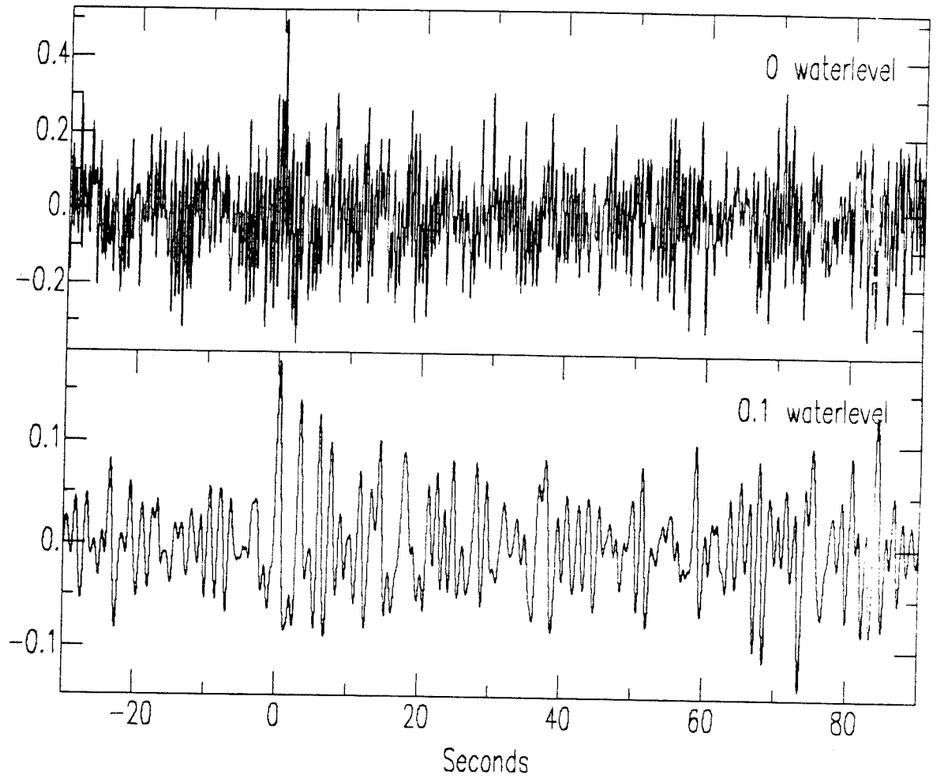

Figure 3.4b. Source equalization of event 139 using a Gaussian parameter of 5.0 and waterlevels of 0 (top trace) and 0.1 (bottom trace).

data, only radial data were interpreted. Figure 3.5 displays the radial and vertical seismograms, and radial deconvolved receiver functions for events which were used in the analysis. The locations of these events are included in Table 3.3c.

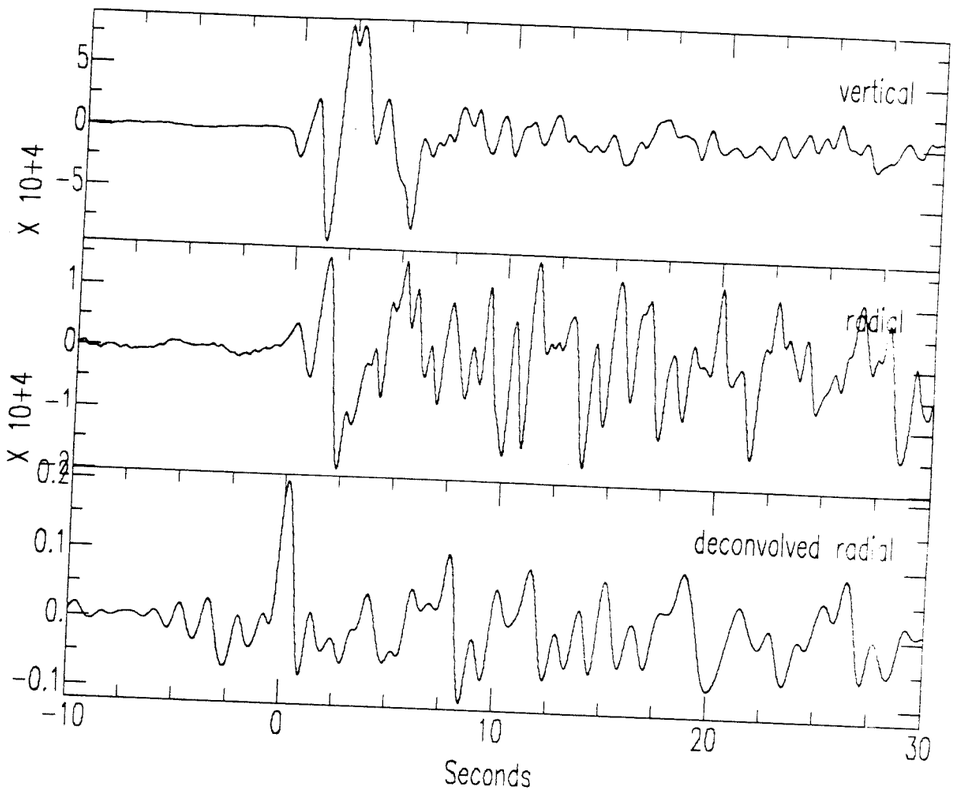

Figure 3.5a. Vertical and radial seismograms, and radial deconvolved receiver function from event 102.

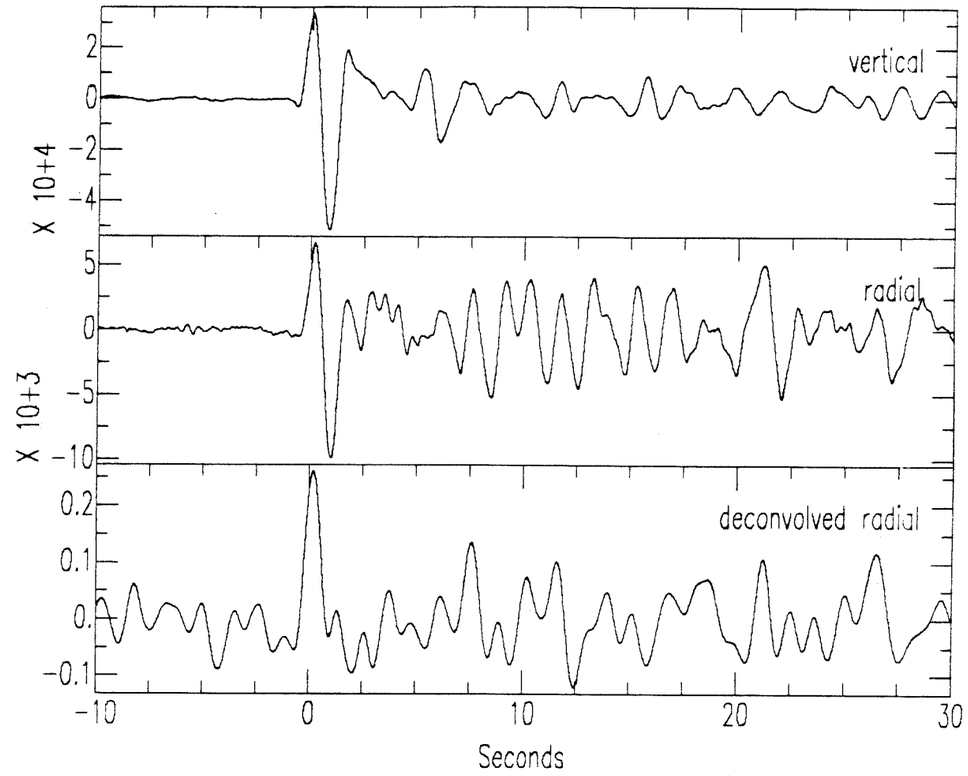

Figure 3.5b. Vertical and radial seismograms, and radial deconvolved receiver function from event 105.

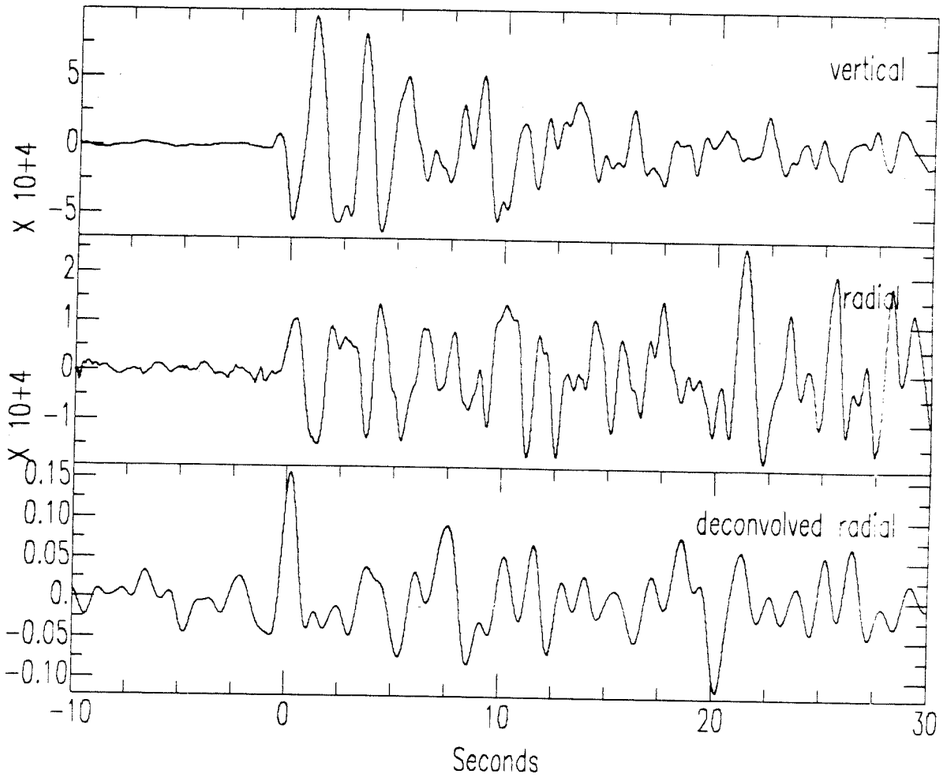

Figure 3.5c. Vertical and radial seismograms, and radial deconvolved receiver function from event 140.

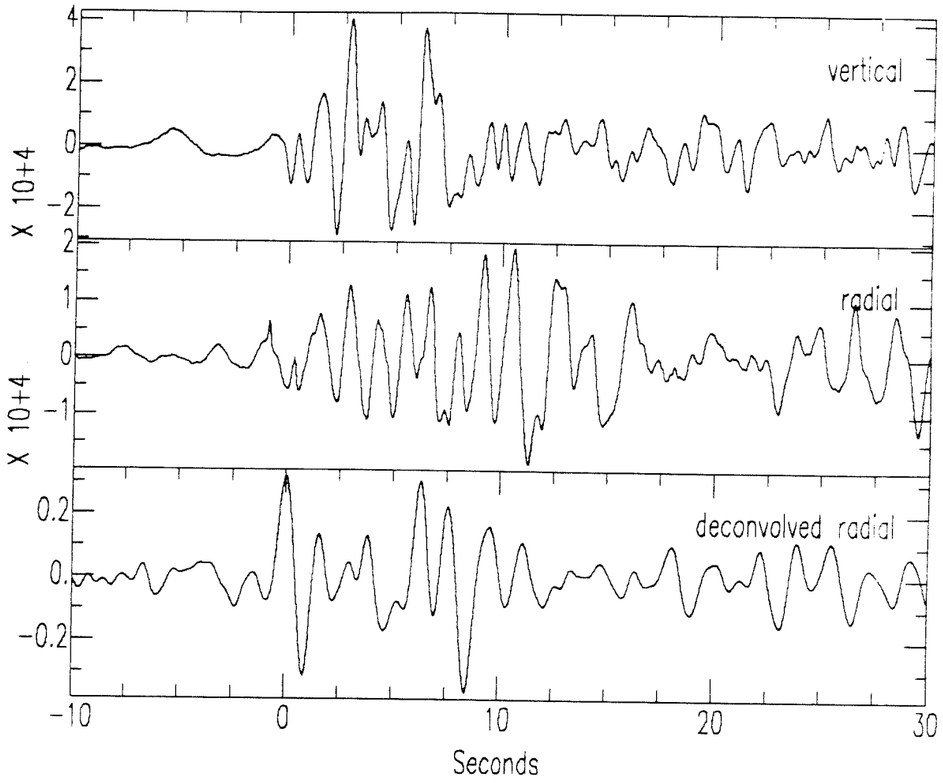

Figure 3.5d. Vertical and radial seismograms, and radial deconvolved receiver function from event 144.

Chapter 4

Analysis

The events from southwest back azimuths used for analysis were event numbers 102, 105, and 140 (see Table 3.3c). These events produced highly similar deconvolved receiver functions and had locations within 5 degrees in both back azimuth and distance. Hence, these deconvolutions were stacked (see Figure 4.1). Event 144 was the only event from a southeast back azimuth to render a high quality radial deconvolved receiver function. However, event 108 rendered a radial deconvolved receiver function of moderate quality from a similar epicentral location (see Table 3.3c). These two southeast back azimuth deconvolutions are displayed in Figure 4.2. The persistent features are seen to be an arrival at close to 4 seconds and large arrivals starting just after 6 seconds. The first of the arrivals after 6 seconds has similar amplitude on the two traces, while the subsequent arrivals exhibit a large variation in amplitude. This confirmation of the persistence of certain arrivals serves as justification for using a single good quality deconvolved receiver function in the analysis.

Figure 4.3 displays the southwest and southeast deconvolutions which were used in the analysis. The ray parameters of the direct *P* waves at the base of the lithosphere were approximately .04 sec/km and .05 sec/km for the southwest and southeast data, respectively. The azimuths and distances of the corresponding events are represented in Figure 4.4. The persistent arrivals addressed by this study are labeled *a*, *b*, *c* and *d* in Figure 4.3. A comparison of the traces in Figure 4.3 reveals some interesting features. Phases *a* and *c* arrive almost simultaneously with amplitudes of 20% and 40% of direct *P*, respectively. Phase *b* arrives

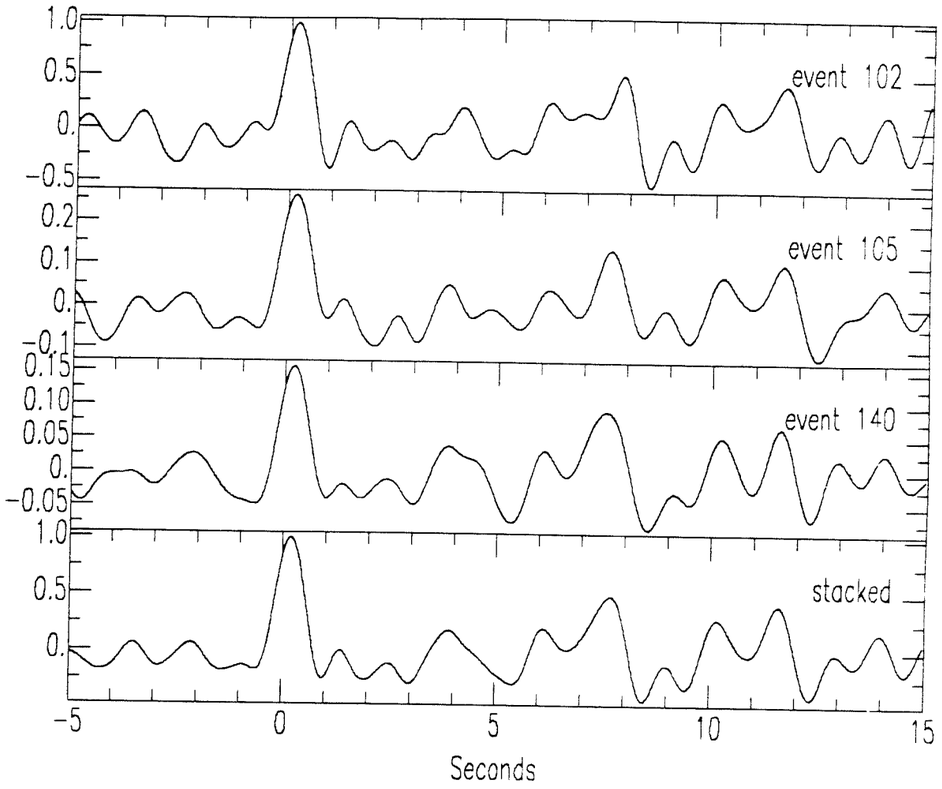

Figure 4.1. Normalized deconvolved receiver functions and stack of events from a southwest back azimuth (230 degrees).

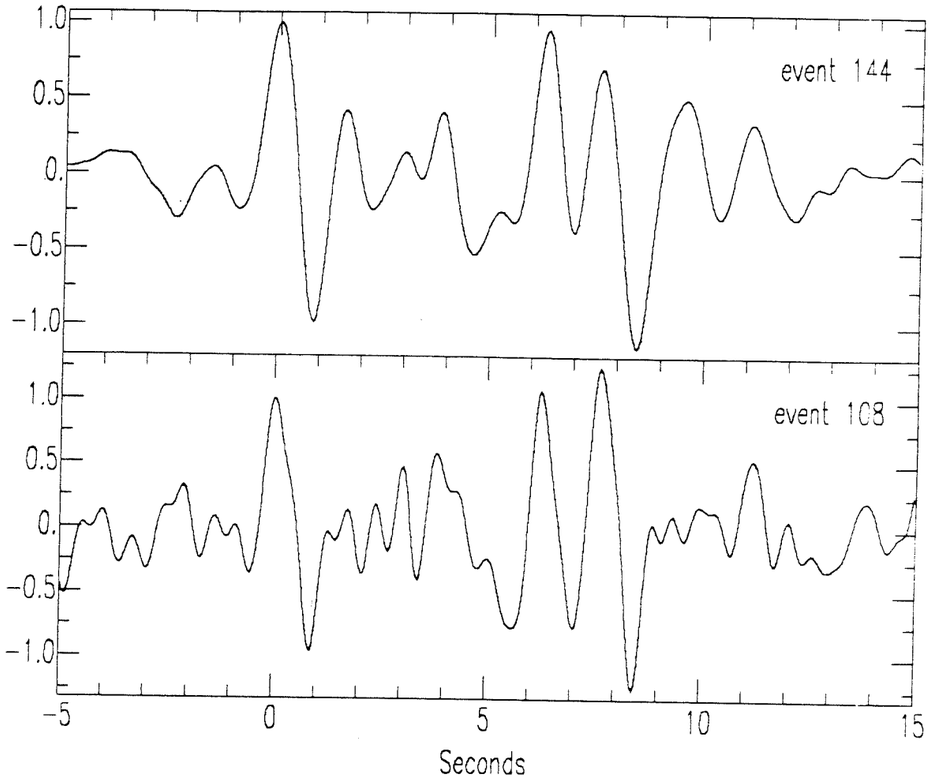

Figure 4.2. Normalized deconvolved receiver functions of events from a southeast back azimuth (130 degrees).

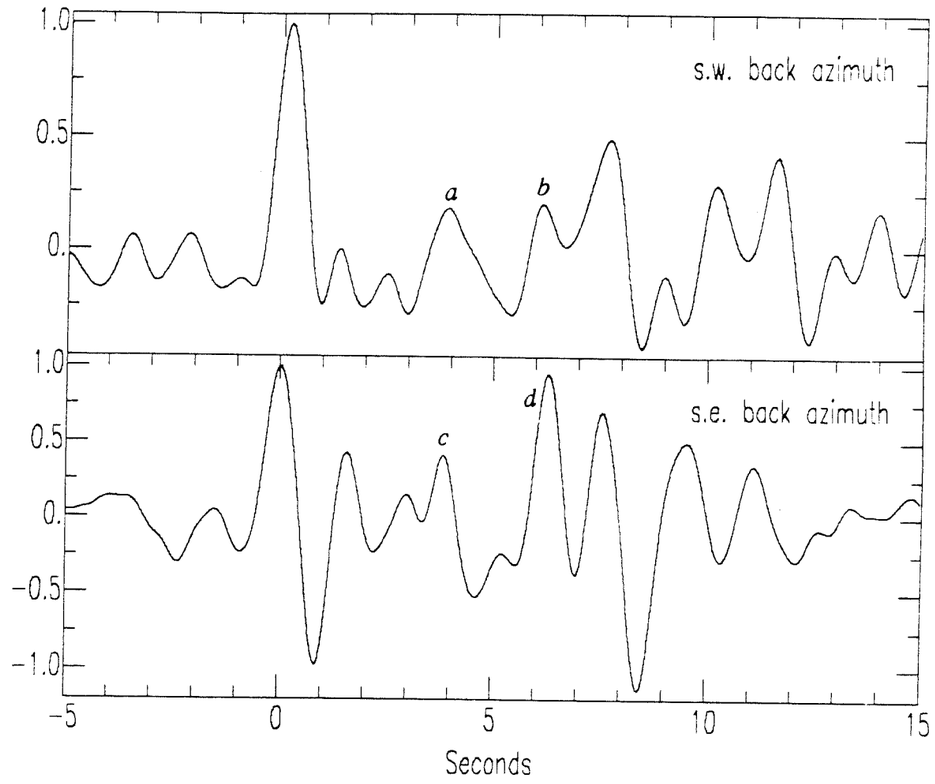

Figure 4.3. Normalized deconvolved receiver functions used in the forward modeling.

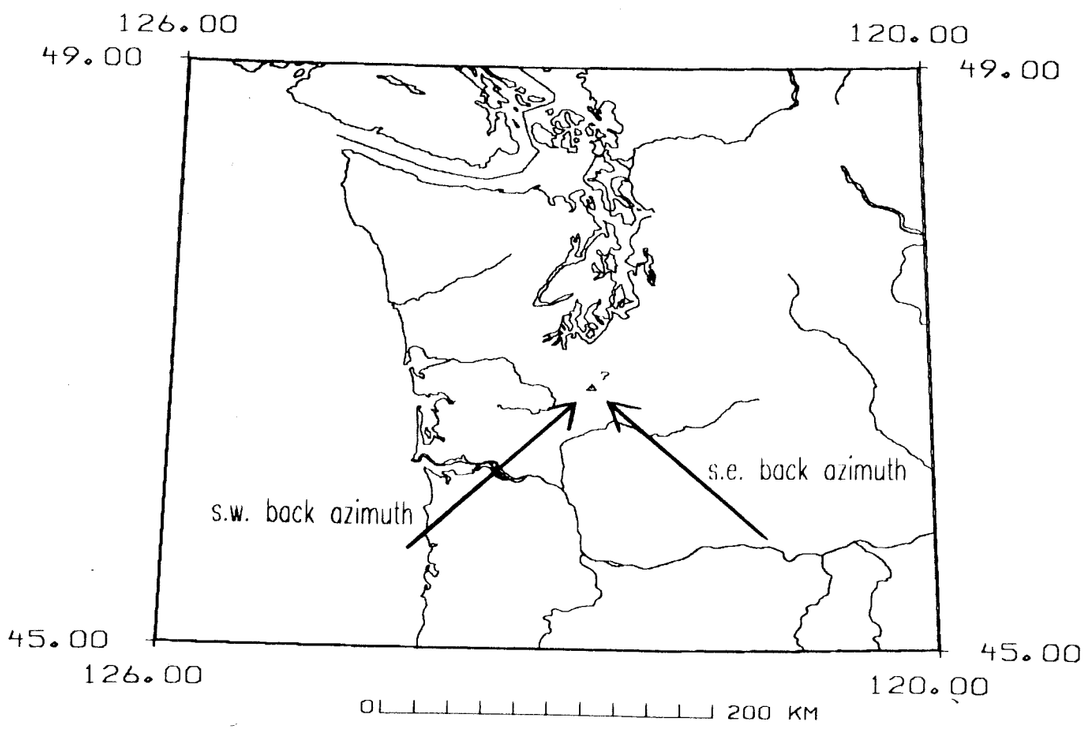

Figure 4.4. Azimuth representation of events used in the forward modeling.

approximately .2 seconds before phase *d* and has considerably smaller amplitude. Forward modeling was performed to reproduce these features.

Prior to investigating features in the data due to sub-surface structure, it was necessary to examine the possibility of complex surface structure. Phases arriving in the first two seconds are generated by very shallow structure (i.e. the upper 2 km). The presence of complicated shallow structure is typically indicated by several clearly observable features in the radial deconvolved receiver functions.

The observation of an azimuth-dependent delay of the direct arrival in a deconvolved radial trace is one indication of complex surface structure. Owens and Crosson (1987) have demonstrated that such a delay is the result of an extremely efficient direct *P* to *S* conversion through a near surface dipping layer. The converted arrival can have sufficient amplitude to dominate over the direct *P* wave, giving the impression of a delay in the first arrival. An apparent delay of .5 seconds can be explained by a shallow interface dipping at roughly 15 degrees. Events from southwest back azimuths rendered radial deconvolved receiver functions with the largest apparent direct *P* delay (see Figure 4.3). The southwest back azimuth data show apparent direct *P* delays of less than .2 seconds. As illustrated by Figure 4.5, a near-surface interface (see Table 4.1) dipping 3 degrees to the southwest reproduces the observed azimuth-dependent first arrival delay. This small amount of surface layer dip may explain the differences observed in the early part (i.e. the first 2 seconds) of the southeast and southwest data. However, synthetic examples showed that the effect of such a small amount of surface layer dip upon later arrivals is negligible. Hence, surface layer dip was not included in the synthetic structures used for modeling arrivals due to deeper lithospheric structure.

Another indication of shallow complexity is the presence of a persistently large arrival in the first two seconds of the radial deconvolved receiver functions.

Table 4.1

Shallow Dipping Interface Model

layer #	P wave velocity	S wave velocity	density	thickness	strike	dip
	km/sec	km/sec	g/cm^3	km	degrees	degrees
1	3.0	1.73	2.20	1.3	160.0	3.0
2	5.1	2.94	2.60			

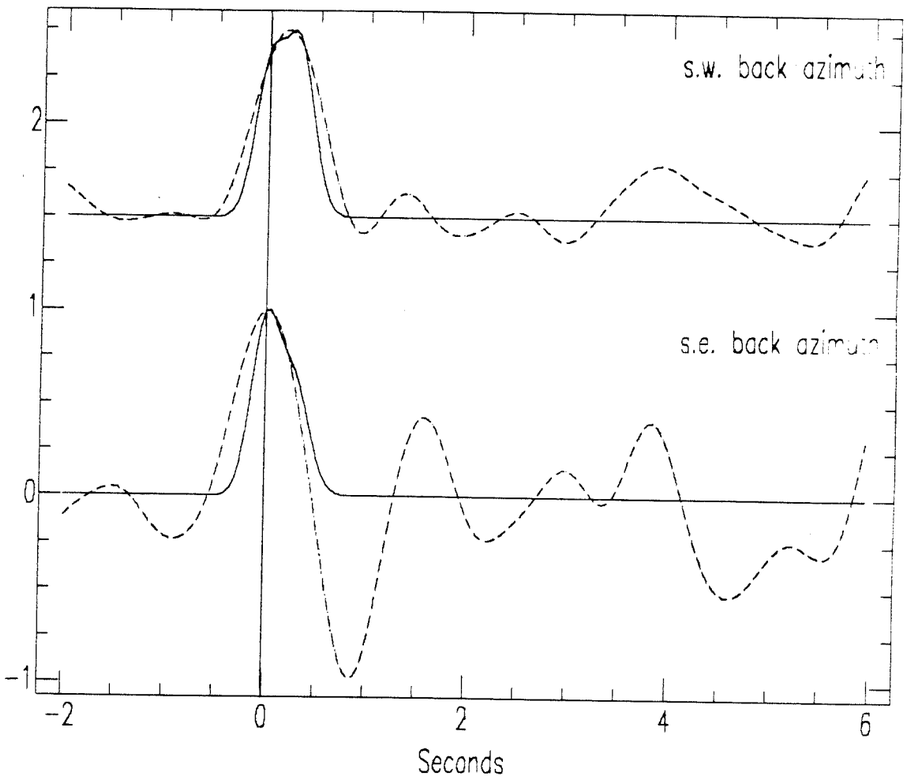

Figure 4.5. Synthetic reproduction (solid traces) of apparent first arrival delay in the real data (dashed traces) using a shallow dipping interface (Table 4.1).

Such arrivals are generated by a high contrast shallow interface. Figure 4.6 displays a record section of data recorded at site 6 (see Figure 3.1). Note the persistence of the large arrival at approximately 1.7 seconds. This large early arrival is strong evidence for a shallow high contrast flat interface beneath site 6. Later portions of the data will be contaminated by reverberated phases due to this shallow high contrast interface. A possible source of shallow complexity beneath site 6 is the presence of Quaternary deposits overlying the basement basalts (Cowan and Potter, 1986). Data recorded at site 7 do not display this type of persistently large early arrival. Thus, the contamination of later arrivals due to shallow complexity was not a major concern in the analysis of data recorded at site 7.

In order to interpret the features of the data attributable to sub-surface structure, it was necessary to investigate the likelihood of certain phases being persistently observed in the deconvolution. In a complex structural environment such as the Pacific northwest, the raypaths traversed by phases which are reverberated by deep structure are highly back azimuth dependent. One can expect that these reverberated phases will be much less persistently observed than direct converted arrivals (Langston, 1981). Hence, persistent arrivals in the deconvolved data resulting from sub-surface structure were interpreted as direct conversions. A confirmation of this interpretation by comparison of radial to vertical seismograms (see Chapter 2) was not possible because of blurring due to source effects.

Because of the absence of evidence supporting severe shallow structure, the persistent arrivals observed in the deconvolved data displayed in Figure 4.3 were interpreted as uncontaminated direct *P* to *S* conversions. As stated previously, forward modeling was based on trial-and-error matching of persistently observed features in the deconvolved radial data. The initial velocity model used was based on the model employed by Owens *et al.* (1987a). The lithospheric seismic velocities in this model incorporate the results of several regional seismic studies of the

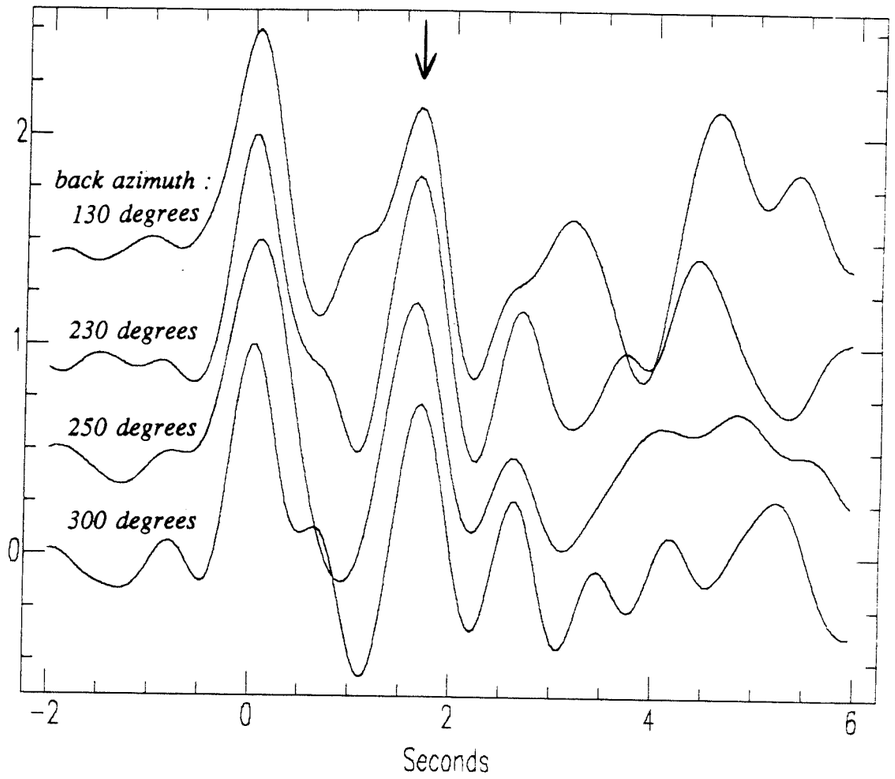

Figure 4.6. Site 6 record section displaying a large early arrival indicative of severe shallow structure.

lithosphere (Taber and Smith, 1985; Zervas and Crosson, 1986; Taber and Lewis, 1986). The essential features of this velocity model are an average crustal *P*-wave velocity of 5.9 km/sec and a contrast of 1 km/sec at the Moho. The model includes an upper mantle half-space with a *P*-wave velocity of 8.0 km/sec. The v_p/v_s ratio of approximately 1.73 used in the construction of this model has been constrained by the analysis of local travel time data (Crosson, personal communication). Errors resulting from the use of improper *S*-wave velocities are unlikely.

The nearly simultaneous arrival times and similar amplitudes of arrivals *a* and *c* led to their interpretation as direct conversions through a flat layer. The difference in amplitude of these arrivals was attributed largely to differences in ray parameter. On the basis of the relative timing of arrivals *a* and *c* (i.e. with respect to direct *P*), the refracting interface must be at a depth of roughly 30 km. Arrivals *a* and *c* were reproduced by using the synthetic crustal structure listed in Table 4.2. The interface responsible for arrivals *a* and *c* was inferred to be at a depth of 30.8 km. This interface was interpreted as the continental Moho. Figure 4.7 displays the synthetic reproduction of arrivals a and c.

No attempt was made to reproduce the arrivals preceding arrivals *a* and *c*. The first three seconds of data consists of small arrivals due to low contrast interfaces and one larger arrival at 1.6 seconds in the southeast back azimuth deconvolution (see Figure 4.3). Adjusting the crustal structure to reproduce the small early arrivals with synthetic direct conversions would have very little effect on the deeper structure. For example, the effect of adjusting the crustal model to reproduce the 2.9 second arrival in the southeast back azimuth deconvolution (see Figure 4.7) would be a change in continental Moho depth of less than 1 km. The 1.6 second arrival in the southeast back azimuth deconvolution is not a persistent feature and is likely due to contamination by *P* energy (see Chapter 2).

Table 4.2

Crustal Model

layer #	P wave velocity	S wave velocity	density	thickness	strike	dip
	km/sec	km/sec	g/cm^3	km	degrees	degrees
1	3.0	1.73	2.20	1.3		0.0
2	5.1	2.94	2.60	3.0		0.0
3	5.9	3.41	2.70	5.0		0.0
4	6.3	3.60	2.75	8.0		0.0
5	6.7	3.87	2.80	13.5		0.0
6	7.7	4.45	3.0			

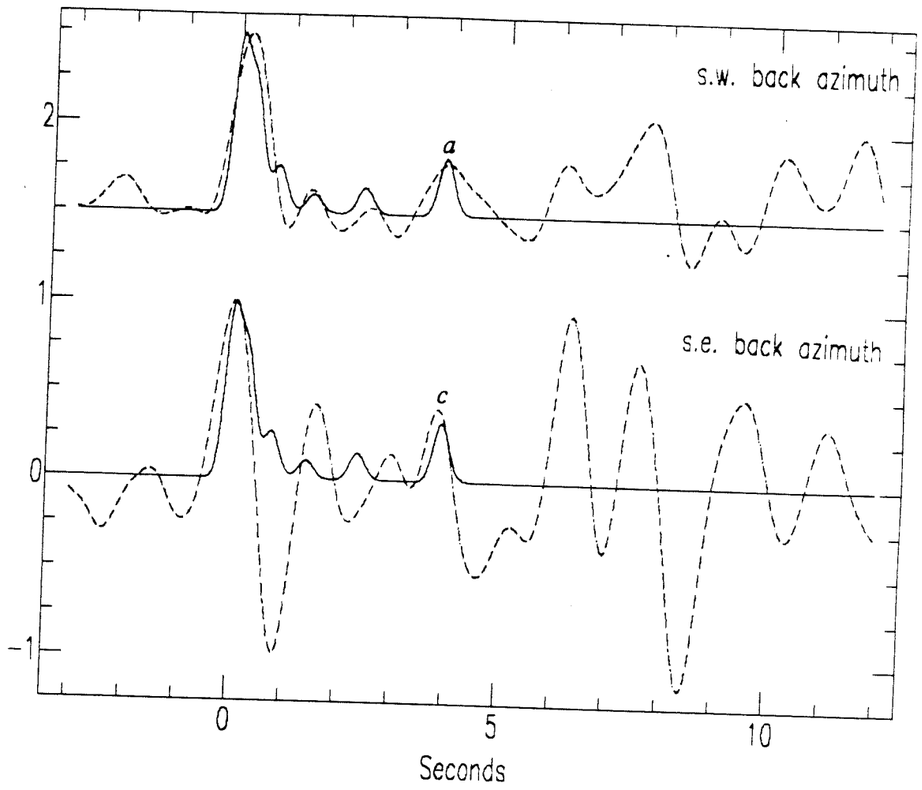

Figure 4.7. Synthetic reproduction (solid traces) of arrivals *a* and *c* in the real data (dashed traces) using crustal model (Table 4.2).

The average crustal velocity of 5.9 km/sec in the model employed by this study represents a somewhat lower value than those suggested for other regions of western Washington. Typical values range up to approximately 6.6 km/sec (Crosson, 1976). Constraint was placed on the local depth of the continental Moho by matching the timing of arrivals *a* and *c* using constant crustal velocities representing end-member average values. The result of this exercise was an inferred local continental Moho depth of 30.8 km ± 3 km. It was necessary to confirm that the synthetic data were highly sensitive to such a range of continental Moho depths. The depth of the synthetic interface in Table 4.2 interpreted as the continental Moho (i.e. the interface separating layers 5 and 6) was perturbed by ± 3 km. The effect of this perturbation on the synthetic match of arrivals *a* and *c* is displayed in Figure 4.8. Arrivals *a′* and *c′* resulted from decreasing the depth of the interface by 3 km and arrivals *a″* and *c″* resulted from deepening the interface by 3 km. Clearly, the suggested depth range of 30.8 km ± 3 km for the continental Moho is a liberal constraint with regard to the timing of arrivals *a* and *c*.

The modeling of arrivals *b* and *d* was somewhat more involved. The amplitude of arrival *d* (90% of direct the *P* wave) is a clear indication of dipping structure. Such large arrivals are not observed in regions of vertically heterogeneous structure (Owens *et al.*, 1987a; Owens *et al.*, 1987b). Synthetic examples indicate that dipping structure can result in a considerable azimuthal variation in the amplitude of direct converted arrivals (see Figure 2.3). In order to model arrivals *b* and *d* as direct arrivals converted by the same dipping interface, deeper layers were added to the structure listed in Table 4.2. The arrival times of phases *b* and *d* indicate an interface at a depth of roughly 50 km beneath site 7. In order to reproduce the amplitude of arrival *d* with a direct conversion through a synthetic interface having a velocity contrast of up to 1 km/sec , the interface would need to be dipping in excess of 60 degrees. It would not be possible to match both arrivals *c*

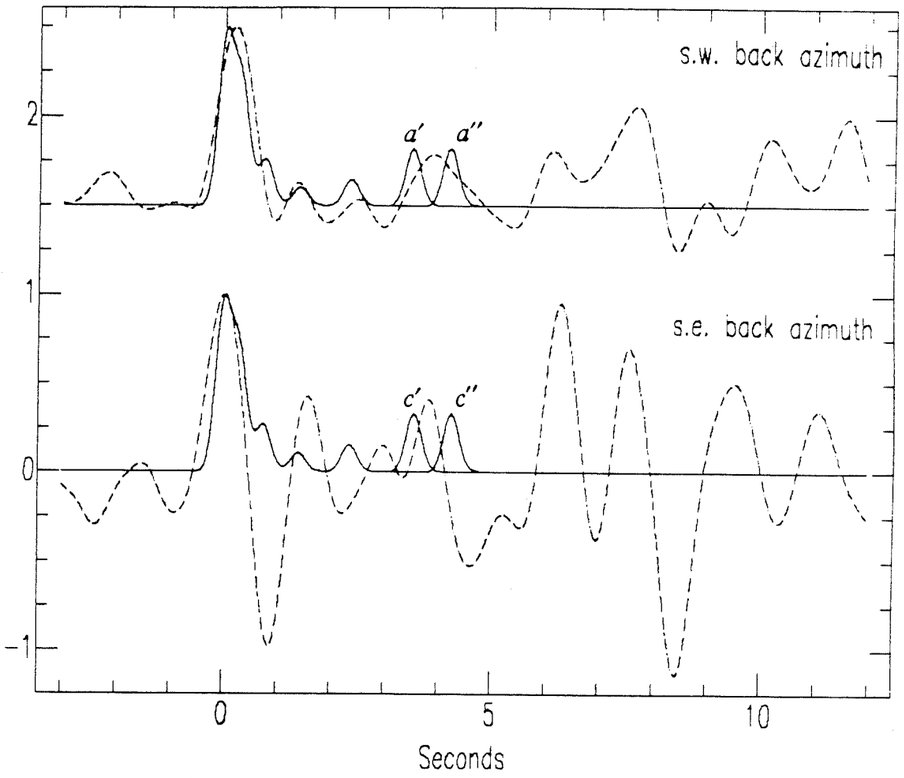

Figure 4.8. Effect of continental Moho depth perturbation (± 3 km) upon the synthetic reproduction (solid traces) of arrivals *a* and *c* in the real data (dashed traces). See text for explanation of synthetic arrivals.

and *d* using such excessive dips. In order to reproduce the amplitude of arrival *d* using more modest dips, it was necessary to employ a synthetic dipping layer having anomalously low velocity. Both increased dip and increased velocity contrast enhance the amplitude of a direct updip converted arrival. The large velocity contrast associated with such a low velocity layer allowed dips to be more reasonable in the synthetic structure. Arrivals *b* and *d* were interpreted as direct *P* to *S* conversions through the bottom interface of this layer. Strike and dip were adjusted in order to reproduce these arrivals. The preferred lithospheric model is listed in Table 4.3. Figure 4.9 displays the reproduction of arrivals *a*, *b*, *c*, and *d* by synthetic data generated using this model. The dipping low velocity layer was interpreted as the crust of the subducted JDF plate. The oceanic crust was inferred to have a local dip of 16 degrees striking *N35E*. The oceanic Moho (i.e. the lower boundary of the subducted oceanic crust) was inferred to have a local depth of 53.8 km.

In order to constrain the suggested geometry of the subducted oceanic crust, the sensitivities of the synthetic data to small changes in the lithospheric model were investigated. Constraint on the depth of the oceanic Moho took into account the previously determined end-member continental Moho depths in a liberal fashion. Increasing the continental Moho depth forces a decrease in the absolute depth of the oceanic Moho in order to preserve the timing of arrivals *b* and *d*. Similarly, a decreased continental Moho depth requires an increased oceanic Moho depth. Thus, in order to produce the most liberal constraint on local oceanic Moho depth, shallow and deep end-member oceanic Moho depths were investigated using the previously determined deep and shallow end-member continental Moho depths, respectively. The results were bounds of ± 5 km on the depth of the oceanic Moho. Figure 4.10 displays the arrivals resulting from the end-member oceanic Moho depths along with the arrivals generated by the end-member continental

Table 4.3

Lithospheric Model

layer #	P wave velocity	S wave velocity	density	thickness	strike	dip
	km/sec	km/sec	g/cm^3	km	degrees	degrees
1	3.0	1.73	2.20	1.3		0.0
2	5.1	2.94	2.60	3.0		0.0
3	5.9	3.41	2.70	5.0		0.0
4	6.3	3.60	2.75	8.0		0.0
5	6.7	3.87	2.80	13.5		0.0
6	7.7	4.45	3.00	17.0	35.0	16.0
7	6.7	3.87	2.80	6.0	35.0	16.0
8	8.0	4.62	3.36			

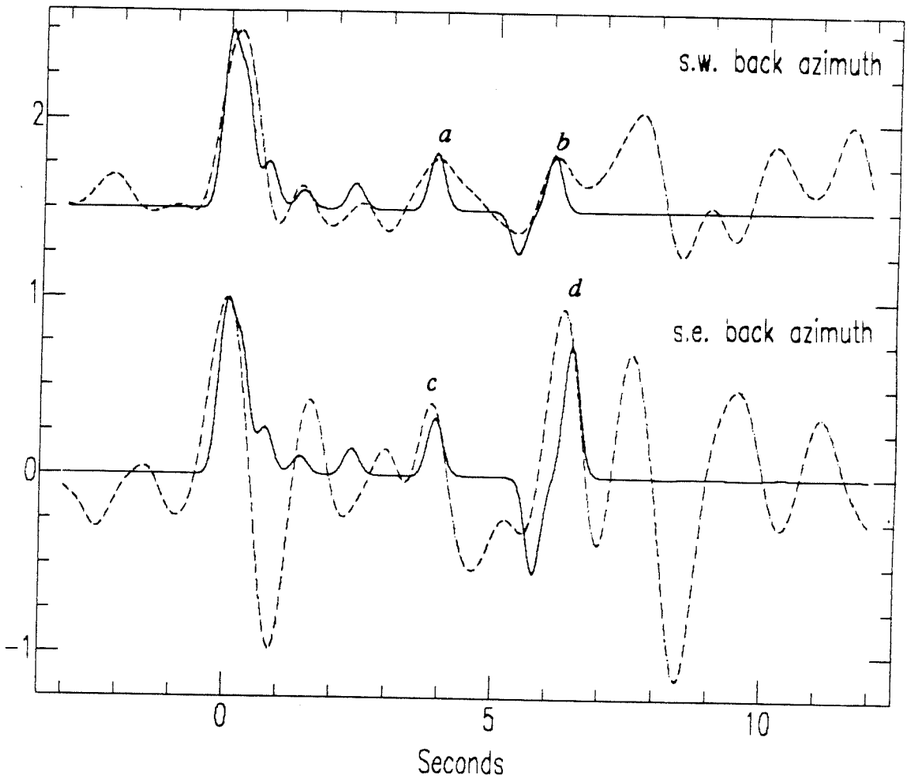

Figure 4.9. Synthetic reproduction (solid traces) of arrivals *a*, *b*, *c* and *d* in the real data (dashed traces) using lithospheric model (Table 4.3).

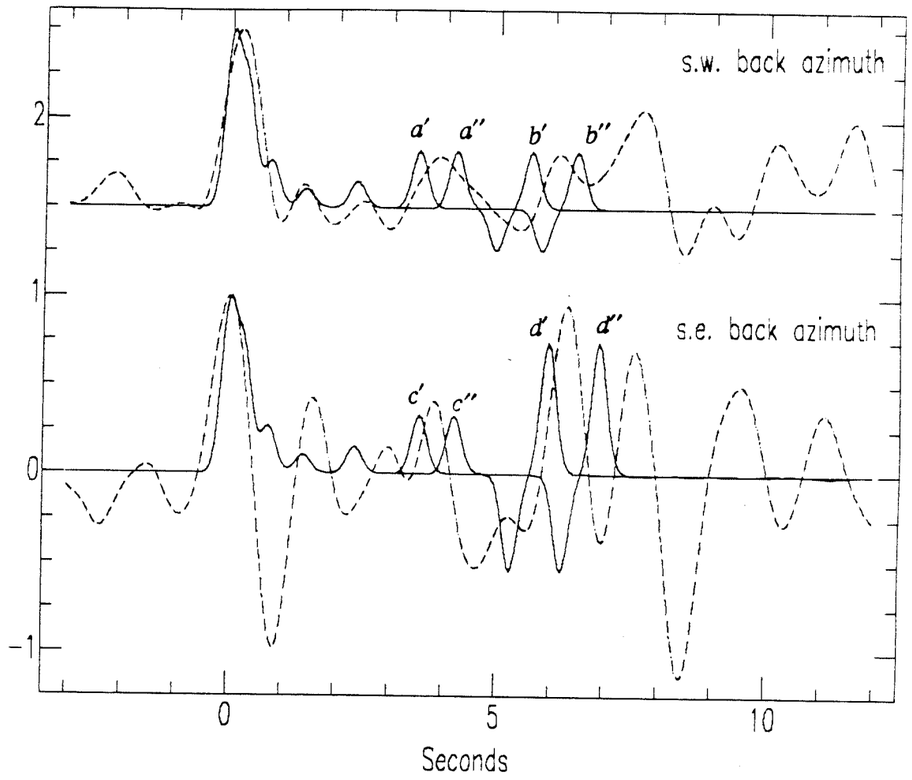

Figure 4.10. Effect of oceanic Moho depth perturbation (± 5 km) upon the synthetic reproduction (solid traces) of arrivals *b* and *d* in the real data (dashed traces). See text for explanation of synthetic arrivals.

Moho depths. Arrivals a', a'', b' and b'' are associated with the end-member continental Moho depths (see above). Arrivals b' and d' correspond to the deep end-member oceanic Moho depth (using the shallow end-member continental Moho depth). Arrivals b'' and d'' correspond to the shallow end-member oceanic Moho depth (using the deep end-member continental Moho depth).

While arrival time is particularly sensitive to layer depth, amplitude is sensitive to orientation (i.e. strike and dip). The sensitivity of the synthetic reproduction of arrivals b and d to the orientation of the dipping low velocity layer in the lithospheric model (see Table 4.3) was investigated, resulting in constraints on the local strike and dip of the subducted oceanic crust. Local end-member strikes and dips of the subducted oceanic crust were determined by perturbing the preferred orientation of the synthetic low velocity layer interpreted as the subducted oceanic crust. Synthetic reproductions of arrivals b and d corresponding to models with end-member strikes and dips displayed a larger range of amplitudes than the real data. Hence, the resulting constraints are quite liberal. The results of this perturbation were a strike of $N35E \pm 15$ degrees and a dip of 16 degrees $\pm$ 5 degrees.

The geometry of modestly dipping structure (both at the surface and at depth) can be well constrained if an extensive high quality data set is available. Critical information regarding the strike of dipping layers is contained within the tangential data. However, the extensive azimuthal coverage of high quality tangential data necessary in order to extract this information was not obtained. In addition, improved azimuthal coverage of high quality radial data would have improved the constraint on dip. Although such tight constraints were not possible, the lithospheric structure inferred from persistent features in the data was constrained well enough to be useful in further interpretation.

Chapter 5

Discussion

Source equalized radial seismograms were used to model the local subduction geometry south of Puget Sound. Persistently observed arrivals interpreted as direct *P* to *S* conversions were reproduced. The synthetic model responsible for the best reproduction of these arrivals (see Table 4.3) represents the suggested local subduction geometry. This model incorporates continental and oceanic Moho v_p contrasts of 1.0 km/sec and 1.3 km/sec, respectively, and an average crustal *P*-wave velocity of 5.9 km/sec. *S*-wave velocities are approximately 1.73 times *P*-wave velocities. The local depth to the continental Moho was constrained by reproducing the timing of direct *P* to *S* conversions through the continental Moho using regional end-member average crustal velocities. The resulting constraints were shown to be consistent with constraints based on perturbations to the synthetic crustal thickness. In addition, the effect of perturbing the synthetic oceanic Moho depth upon the reproduction of direct *P* to *S* conversions through the oceanic Moho was investigated, resulting in constraints on the local depth to the oceanic Moho. The local lithospheric model is summarized as follows :

continental moho depth = 31 *km* ± 3 *km*

oceanic moho depth = 54 *km* ± 5 *km*

oceanic crust strike = *N*35*E* ± 15 *degrees*

oceanic crust dip = 16 *degrees* ± 5 *degrees*

Owens *et al.* (1987a) have investigated the local subduction geometry approximately 60 km west of the station analyzed by this study. The local results

of Owens *et al.* (1987a) and this study are consistent with a large scale model of subduction beneath western Washington. The sites analyzed by Owens *et al.* (1987a) and this study are displayed in Figure 5.1. Figure 5.2 compares the southeast back azimuth data used by Owens *et al.* (1987a) to the data used in this study. Owens *et al.* (1987a) interpreted arrivals *C* and *D* as direct conversions through the continental and oceanic Mohos, respectively. The interpretation of arrivals *c* and *d* as direct conversions through the continental and oceanic Mohos, respectively, is discussed in Chapter 4.

The similar timing of arrivals *c* and *C* (i.e. approximately 4 seconds after direct *P*) reinforce their interpretation as direct conversions through a flat continental Moho (Zervas and Crosson, 1986) having a somewhat shallower depth than suggested by Crosson (1976) (i.e. 31 km as opposed to 41 km). Future studies should attempt to solve this discrepancy.

Arrival *D* is observed at an earlier time in the data than arrival *d*. The observed move-out of arrivals *D* and *d* across the two sites is consistent with their interpretation as conversions through the subducted oceanic Moho. Owens *et al.* (1987a) suggest an oceanic crust with a local dip of 20 degrees ± 3 degrees, a strike of *N20E* ± 20 degrees and a bottom interface (i.e. the oceanic Moho) at a depth of 38 km. Using a strike of *N25E* and the oceanic Moho depths from Owens *et al.* (1987a) and this study, a true dip of 15 degrees was extrapolated between the two data collection sites. Changing the slab strike and local (i.e. to site 7) oceanic Moho depth by ± 15 degrees and ± 5 km, respectively, resulted in extrapolated dips within the range of 16 degrees ± 5 degrees suggested by this study.

The results of Owens *et al.* (1987a) were a vital piece of evidence in support of the new 3-dimensional model of the subducted JDF plate proposed by Crosson and Owens (1987). The depth contours of the oceanic Moho suggested by

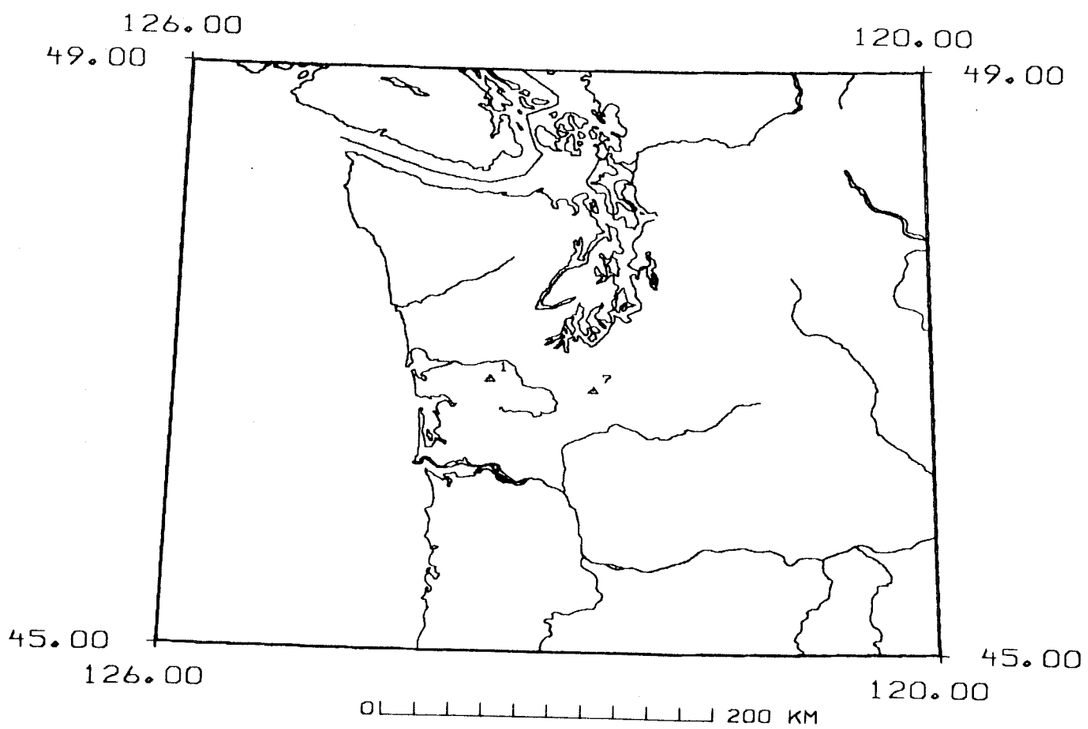

Figure 5.1. Locations of sites 1 and 7 used by Owens *et al.* (1987b) and this study, respectively.

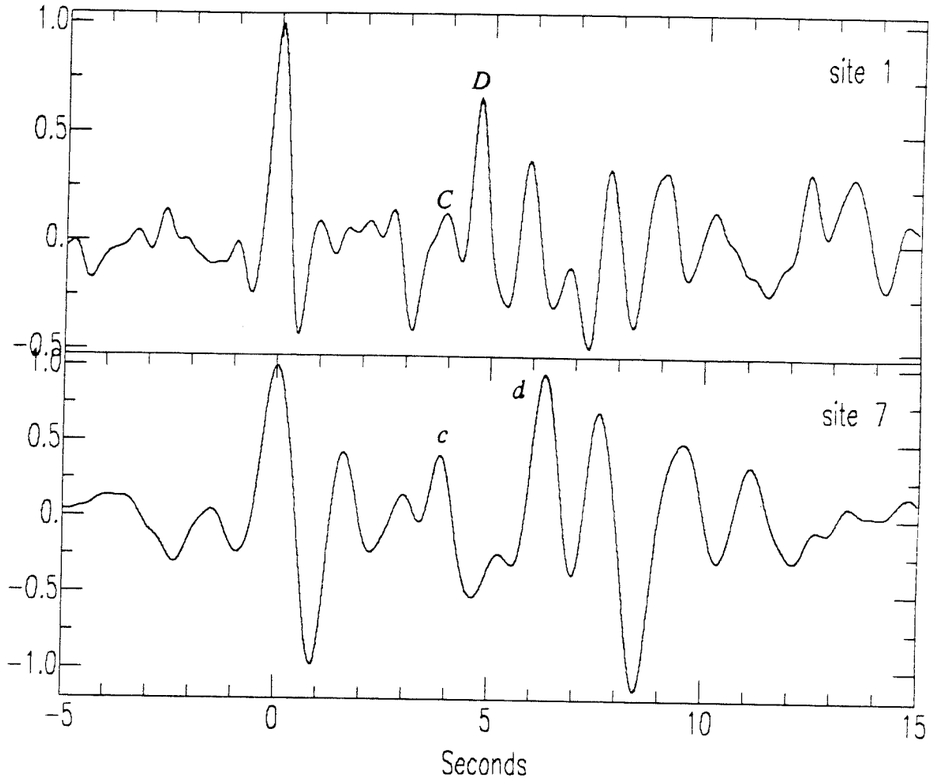

Figure 5.2. Deconvolutions of data from a southeast back azimuth (130 degrees) analyzed by Owens *et al.* (1987b) (top trace) and this study (bottom trace).

Crosson and Owens (1987) predict an oceanic Moho depth of between 50 and 60 km beneath the site analyzed in this study. This is consistent with the local depth of approximately 54 km suggested by this study. The slab geometry suggested by Crosson and Owens (1987) places the site analyzed by this study above the southern flank of the subducted slab's arch. The southwest dip direction and relatively large dip (i.e. in comparison to Puget Sound) suggested by this study are consistent with this suggested site location with regard to the the slab.

Our knowledge of the subduction geometry beneath western Washington is just developing. This study has provided local constraints on this geometry in a region of southwest Washington south of Puget Sound. As the present data set expands, further analysis will improve the results presented here. By relocating our broadband stations to various sites in southwest Washington, additional constraints on local slab geometry will be developed. These constraints will serve to test and refine the new 3-dimensional model of the subducted JDF plate (Crosson and Owens, 1987) and other large scale models of subduction in the Pacific northwest.

BIBLIOGRAPHY

Ammon, C. J., Time domain teleseismic *P*-waveform modeling and the crust and upper mantle structure beneath Berkeley, California, M.S. thesis, State Univ. of N.Y. , Binghamton, 1985.

Aki, K., and P. G. Richards, *Quantitative Seismology,* W. H. Freeman and Company, San Francisco, 1980.

Atwater, T., Implications of plate tectonics for the Cenozoic tectonic evolution of western North America, *Geol. Soc. Am. Bull.,* **81**, 3513-3536, 1970.

Burdick, L. J., and C. A. Langston, Modeling crustal structure through the use of teleseismic body-wave forms, *Bull. Seis. Soc. Am.,* **67**, 677-691, 1977.

Carlson, R. L., Cenozoic plate convergence in the vicinity of the Pacific Northwest: a synthesis and assessment of plate tectonics in the northeastern Pacific, Ph.D. dissertation, Univ. of Wash., Seattle, 1976.

Carson, B. J., J. Yuan, P. B. Meyers, Jr., and W. D. Barnard, Initial deep-sea sediment deformation at the base of the Washington continental slope: a response to subduction, *Geology,* **2**, 561-564, 1974.

Clayton, R. W., and R. A. Wiggins, Source shape estimation and deconvolution of teleseismic bodywaves, *Geophys. J. R. Astr. Soc.,* **47**, 151-177, 1976.

Cowan, D. S., and C. J. Potter, Continent-ocean transect B3: Juan de Fuca spreading ridge to Montana thrust belt, *Geol. Soc. Am., 1986.*

Crosson, R. S., Crustal structure modeling of earthquake data 2. Velocity structure of the Puget Sound region, Washington, *J. Geophys. Res.*, **81**, 3047-3054, 1976.

Crosson, R. S., Review of seismicity in the Puget Sound region from 1970 through 1978, in *Procedings of Workshop XIV, Earthquake Hazards of the Puget Sound Region, Washington,* edited by J. C. Yount, 1983. USGS open file report, 83-19.

Crosson, R. S., and T. J. Owens, Slab geometry of the Cascadia subduction zone beneath Washington from earthquake hypocenters and teleseismic converted waves, *Geophys. Res. Lett.*, In press, 1987.

Green, A. G., R. M. Clowes, C. J. Yorath, C. Spencer, E. R. Kanasewich, M. T. Brandon, and A. S. Brown, Seismic reflection imaging of the subducting Juan de Fuca plate, *Nature,* **319**, 210-213, 1986.

Helmberger, D. and R. A. Wiggins, Upper mantle structure of the Midwestern United States, *J. Geophys. Res.*, **76**, 3229-3245, 1971.

Hendrickson, M. A., The determination of seismic structure from teleseismic *P* waveforms on the Washington continental margin, M.S. thesis, Univ. of Wash., Seattle, 1986.

Keach, R. W., C. J. Potter, J. E. Oliver, and L. D. Brown, Cenozoic active margin and shallow Cascades structure: COCORP results from western Oregon (abstract), *GSA Annual Meet.*, **652**, 1986.

Langston, C. A., Corvallis, Oregon, crustal and upper mantle receiver structure from teleseismic *P* and *S* waves, *Bull. Seis. Soc. Am.*, **67**, 713-724, 1977a.

Langston, C. A., The effect of planar dipping structure on source and receiver responses for constant ray parameter, *Bull. Seis. Soc. Am.*, **67**, 1029-1050, 1977b.

Langston, C. A., Structure under Mount Rainier, Washington, inferred from teleseismic body waves, *J. Geophys. Res.*, **84**, 4749-4762, 1979.

Langston, C. A., Evidence for the subducting lithosphere under southern Vancouver Island and western Oregon from teleseismic *P* wave conversions, *J. Geophys. Res.*, **86**(B5), 3857-3866, 1981.

Langston, C. A. and D. E. Blum, The April 29, 1965, Puget Sound earthquake and the crustal and upper mantle structure of western Washington *Bull. Seis. Soc. Am.*, **67**, 693-711, 1977.

Michaelson, C. A., and C. S. Weaver, Upper mantle structure from teleseismic *P*-wave arrivals in Washington and northern Oregon, *J. Geophys. Res.*, **91**, 2077-2093, 1986.

Oldenberg, D. W., A comprehensive solution to the linear deconvolution problem, *Geophys. J. R. Astr. Soc.*, **65**, 331-357, 1981.

Owens, T. J., and R. S. Crosson, Shallow structure effects on broadband teleseismic *P*-waveforms, *Bull. Seis. Soc. Amer.*, In press, 1987.

Owens, T. J., R. S. Crosson, and M. A. Hendrickson, Constraints on the subduction geometry beneath western Washington from teleseismic waveform modeling, *Bull. Seis. Soc. Amer.*, In preparation, 1987a.

Owens, T. J., S. R. Taylor, and G. Zandt, Isolation and enhancement of the response of local seismic structure from teleseismic *P*-waveforms, Lawrence Livermore National Laboratory, Rep. UCID-19809, 33 pages, 1983a.

Owens, T. J., S. R. Taylor, and G. Zandt, Crustal structure beneath RSTN stations inferred from teleseismic *P*-waveforms: Preliminary results at RSCP, RSSD, and RSNY, Lawrence Livermore National Laboratory, Rep. UCID-19859, 28 pages, 1983b.

Owens, T. J., S. R. Taylor, and G. Zandt, Crustal structure at regional stations determined from inversion of broadband teleseismic *P* waveforms, *Bull. Seis. Soc. Amer.*, **77**, 631-662, 1987b.

Owens, T. J., G. Zandt, and, S. R. Taylor, Seismic evidence for an ancient rift beneath the Cumberland Plateau, TN: a detailed analysis of broadband teleseismic *P*-waveforms, *J. Geophys. Res.*, **89**, 7783-7795, 1985.

Riddihough, R. P., Gravity and structure of an active margin - British Columbia and Washington, *Can. J. Earth Sci.*, **16**, 350-363, 1979.

Riddihough, R. P., Recent movements of the Juan de Fuca plate system, *J. Geophys. Res.*, **89**(B8), 6980-6994, 1984.

Taber, J. John, and B. T. R. Lewis, Crustal structure of the Washington continental margin from refraction data, *Bull. Seis. Soc. Amer.*, **76**, 1011-1024, 1986.

Taber, J. John, and S. W. Smith, Seismicity and focal mechanisms of the Juan de Fuca plate beneath the Olympic Peninsula, Washington, *Bull. Seis. Soc. Amer.*, **75**, 237-249, 1985.